PSE PRESS

# CSChE Systems & Control Transactions

## VOLUME 2

Selected Extended Abstracts from the
Systems & Control Division Sessions of the
72nd Canadian Chemical Engineering Conference

October 23-26, 2022

Vancouver, BC

Edited by Mina Naeini

Chemical Institute of Canada | *For Our Future*
Institut de chimie du Canada | *Pour notre avenir*

http://PSEcommunity.org/LAPSE:2022.0095

# CSChE Systems & Control Transactions

## Vol 2

*Edited by*

**Mina Naeini, PhD**
McMaster University

PSE PRESS
PSEcommunity.org
PSE Press ● Hamilton

Chemical Institute of Canada | *For Our Future*
Institut de chimie du Canada | *Pour notre avenir*

CSChE Systems & Control Transactions, Volume 2

PSE Press
*Hamilton, Ontario, Canada*



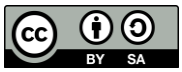

**Living Archive for Process Systems Engineering (LAPSE) Archive ID**
LAPSE:2022.0095

**Library and Archives Canada Catalogue**
A catalogue record and copy of this book is available from Library and Archives Canada

**Archival Permissions**
This book as well as individual articles may be deposited in digital research archives, personal archives, or institutional archives.

Electronic Book
ISBN 978-1-7779403-1-7

10 9 8 7 6 5 4 3 2 1



Typeset in Constantina and Corbel

**Suggested Citations for Individual Articles**
*Paper Style*
Student MC, Supervisor QR. Title of the article. *CSChE Systems & Control Trans*, 2:43-48 (2022).

*Proceedings Style*
Student MC, Supervisor QR. Title of the article. *In: CSChE Systems & Control Transactions*, October 23-26, Vancouver, BC, Canada, 2022. Vol 2 Pages 1-6. ISBN 9781777940317.

**Editor-in-Chief**
Mina Naeini, PhD
*McMaster University*

# Contents

## Preface



## Extended Abstracts

# Introduction

Mina Naeini
*McMaster University*

## The Systems & Control Division

The Canadian Society for Chemical Engineering (CSChE), one of the constituent societies of the Chemical Institute of Canada, is a not-for-profit association made up of chemical engineering professionals, academics, students, and employees of government organizations. The Systems & Control (S&C) division of the CSChE is a collection of members who are interested in process systems engineering (PSE), which includes the design, control, optimization, modelling, simulation, planning, scheduling, and operations of chemical processes.

The S&C Division is an active group with many activities, which include:

(a) The development and management of the Living Archive for Process Systems Engineering, an open-access repository for pre-prints, post-prints, open access articles, research data, simulations, computer code, and other research assets relevant to the field of PSE.

(b) The development of technical standards relevant to the field, such as the development of a new standard on eco-technoeconomic analyses via Standards Council of Canada.

(c) Providing financial supporting for regional conferences relevant to the S&C division

(d) Distribution of relevant announcements and information to our members, such as job postings, new books, and events

## About This Volume

This volume contains selected extended abstracts from the 2022 Canadian Chemical Engineering Conference (CCEC 2022). Five sessions at the conference were managed by the S&C Division, which represent the broad and changing nature of PSE in Canada:

Artificial Intelligence and Machine Learning in Process Systems Engineering
Data Driven Analytics, Control, and Optimization
Industrial Applications in Process Systems Engineering
Methodologies and Fundamentals in Process Systems Engineering
Process Systems Engineering for Energy and the Environment

Prospective contributors submitted short abstracts for either oral presentations or poster presentations for various sessions. Volunteer session co-chairs, who were chosen from the S&C division membership, reviewed each abstract for quality and relevance, and used a ranking system to determine acceptance as an oral presentation or poster, or, rejection. Those who were accepted were invited to contribute an extended abstract to this volume, which contains more information and detail than the original short abstract.

These extended abstracts were not peer reviewed. They generally consist of research-in-progress and early stage research results. In most cases, the information presented herein may be included as a part of a peer-reviewed study in a later publication. For more information about individual works, or to find out about updates, you are encouraged to contact the corresponding author of each study.

Each article has a corresponding LAPSE ID. Visit the LAPSE record to see if the authors have linked their contribution to other material, such as presentation slides, downloadable data, or other publications.

# Chairs and Co-Chairs

## Systems & Control Division Chair

Thomas A. Adams II, *Norwegian University of Science and Technology*

## Session Co-Chairs

**Artificial Intelligence and Machine Learning in Process Systems Engineering**
Yankai Cao, PhD. *University of British Columbia*
Bhushan Gopaluni, PhD. *University of British Columbia*
Nathan Lawrence, MSc. *University of British Columbia*
Prashant Mhaskar, PhD. *McMaster University*
Qinqin Zhu, PhD. *University of Waterloo*
Jingyi Wang, MSc. *University of British Columbia*
Li Zukui, PhD. *University of Alberta*
Siang Lim, BASc. *Georgia Institute of Technology*
Ajay Ray, PhD. *University of Western Ontario*
Kaixun Hua, PhD. *University of British Columbia*

**Data Driven Analytics, Control, and Optimization**
Stevan Dubljevic, PhD. *University of Alberta*
Kaixun Hua, PhD. *University of British Columbia*
Yankai Cao, PhD. *University of British Columbia*
Bhushan Gopaluni, PhD. *University of British Columbia*
Carl Duchesne, PhD. *University of Laval*
Xiang Li, PhD. *Queens University*
Prashant Mhaskar, PhD. *McMaster University*
Debaprasad Dutta, MASc. *Ryerson University*
Xunyuan Yin, PhD. *University of Alberta*

**Industrial Applications in Process Systems Engineering**
Moncef Chioua, PhD. *Polytechnique Montréal*
Jing Wang, BSc. *University of Alberta*
Vladimir Mahalec, PhD. *McMaster University*
Li Feng Zhang, PhD. *University of Saskatchewan*
Nicolas Hudon, PhD. *Queens University*
Simant Upreti, PhD. *Toronto Metropolitan University*

**Methodologies and Fundamentals in Process Systems Engineering**
Kim McAuley, PhD. *Queens University*
Kamil Khan, PhD. *McMaster University*

**Process Systems Engineering for Energy and the Environment**
Luis Ricardez-Sandoval, PhD. *University of Waterloo*
Sohrab Zendehboudi, PhD. *Memorial University*
Thomas A. Adams II, PhD. *Norwegian University of Science and Technology*
Jinfeng Liu, PhD. *University of Alberta*
Ajay Ray, PhD. *University of Western Ontario*
Jiayang Ren, MSc. *University of British Columbia*

*We greatly thank our session chairs and presenters for their time and effort in contributing to this conference!*

CSChE Systems & Control Transactions

Open Access | Original Research

**Conference Proceedings**
Canadian Chemical Engineering Conference 2022
October 23-26, Vancouver, BC, Canada

PSEcommunity.org/LAPSE:2022.0029

PSE PRESS

# GHG Emissions Reduction – Optimal Design and Operation of the Integrated Distributed Energy Systems Cross Different Energy Sectors

**Ruonan Li[a] and Vladimir Mahalec[a]***

[a] McMaster University, Department of Chemical Engineering, Hamilton, Ontario, Canada
* Corresponding Author: mahalec@mcmaster.ca.

## ABSTRACT

This research seeks the opportunity to further reduce the minimum GHG emissions achieved by individually operating energy systems in the civic, industrial, and transportation sectors through their integration. Each entity – buildings or industrial plants, is equipped with a set of combined cooling, heating, and power (CCHP) system. At the same time, there is heat and electricity transfer among entities. The integration intends to solve the mismatch between the energy demand and energy provided by the CCHP system, which further increases the operation of the CCHP system and reduces GHG emissions of the entire system. This research introduces an optimization approach for identifying the optimal design and operation of the integrated system, which provides the maximum GHG emission reduction benefits (represented as GHG emissions reduction percentage (GHGD%)). Compared to existing studies on the integrated system, this research (1) differentiates the temperature of industrial heating demands to ensure feasible heat transfer; (2) optimizes production rates of plants to minimize GHG emissions of the entire system; (3) identifies the optimal relationship between sizes of entities to maximize GHG emissions reduction percentage of the integrated operation. This research implements an integrated system combining entities with different energy demand patterns to balance the supply and demand of heating and electricity. The civic buildings – a residential building and a supermarket that requires more electricity than heating are combined with industrial plants – a confectionery plant, a brewery, and a bakery plant. The confectionery plant and the brewery require more heating than electricity. The bakery plant is investigated under two situations – higher heating than electricity demand and higher electricity demand than heating demand to explore the impacts of changing the energy demand pattern of an entity on GHG emissions reduction benefits of the integrated system. The research also considers the implementation of electric vehicles in the residential building. Results from the case studies indicate that there exist optimal relative entity sizes that lead to a maximum GHGD% of 17.6%. By optimizing the sizes of entities, the highest GHGD% can be maintained at 15.7% - 17.6%, even when the optimal relative entity sizes cannot be followed or there are changes in the energy demand patterns of entities.

**Keywords**: GHG emissions reduction, Cross-sector integration, Optimal design and operation.

**Date Record:** Original manuscript received September 25, 2022. Published October 6, 2022.

## INTRODUCTION

Current research shows that integrating energy systems across different sectors can reduce greenhouse gas (GHG) emissions and improve the efficiency of the entire system [1]. As a typical distributed energy system, the combined cooling, heating, and power (CCHP) system is an efficient solution for integrating different forms of energy.

The CCHP system generates cooling, heating, and electricity locally by burning fuel in its power generation unit (PGU). With multiple types of energy being generated, the operation of an individual CCHP system is generally limited by the lower energy demand to avoid generating excess energy that cannot be used. Thus, outputs of the CCHP system can be limited, even the systems having high efficiencies. Supplementary equipment is implemented beyond the CCHP system to meet the demands of consumers entirely, which generally includes boilers, solar thermal collectors, photovoltaics [2], and electric chillers [3].

A potential solution for the unbalanced energy demand and supply problem is combining CCHP systems of multiple consumers (entities) to form an integrated energy system. Each entity in the integrated system has its own distributed energy system to generate heating, cooling, and electricity locally. Additionally, it performs both as a consumer and

supplier that transfers energy to and receives energy from other entities in the integrated system [4].

This work explores the GHG emission reduction possibility of the integrated system that combines the residential, commercial, industrial, and transportation sectors compared to the individual operating energy systems (the non-integrated system). It addresses the following questions that have not been discussed before: 1. Integrating distributed energy systems of residential, commercial, industrial, and transportation sectors with different energy demand patterns. Temperatures of industrial production processes are differentiated to ensure feasible heat processes. 2. Production rates of the industrial plants are optimized for minimizing GHG emissions of the entire system. 3. Identify the optimal relative entity sizes that maximize GHG emissions reduction benefits of the integrated operation. 4. Explore the impacts of changing the relative entity size and energy demand pattern of entities on GHG emissions reduction of the integrated system.

## OPTIMIZATION PROBLEM FORMULATION

In this work, the GHG emissions reduction benefits of the integrated operation are measured by the GHG emissions reduction percentage (GHGD%). As shown in Eq. (1), it is calculated based on the minimum GHG emissions of the integrated system and the non-integrated system. Therefore, optimization problems have been developed to find the corresponding optimal design and operation of the two systems. The optimal design includes both capacity of each energy system equipment and the size of each entity. The optimal operation contains the amount of energy used and generated by each piece of equipment and the production rates of plants.

$$GHGD\% = \frac{\min GHG_{non-int} - \min GHG_{int}}{\min GHG_{non-int}} \quad (1)$$

### Energy system

#### Energy system description

Each entity in both the integrated system and the non-integrated system has been assumed to have options to install the equipment, as shown in Figure 1.

The power generation unit (PGU) has been assumed as an internal combustion engine that generates electricity by burning fuel. An entity can also connect to the external grid to purchase electricity to fully meet the electricity demand, as well as sell electricity back to the grid for credits. The PGU also generates heat along with electricity. After being recovered by the heat recovery unit, the waste heat is used by the absorption chiller for cooling purposes or used by the heating coil for heating purposes. An entity is also able to install a boiler and an electric chiller for heating and cooling, respectively. For the integrated system, an entity can also receive or dispatch electricity and heat from other entities at a specific time. As for entities of the non-integrated system, the heat and electricity transfer among entities are not available.

Electric vehicles (EVs) are formulated as an aggregated subsystem of the residential building to simplify the formulation. It has been assumed that the EVs can both be charged and discharge electricity when connecting to the energy system of the residential building before 8:00 and after 17:00 daily. All EVs must be fully charged before leaving the building each day.

#### Decision variables

The amount of heating ($Q_{i,t}^{PGU}$) and electricity ($E_{i,t}^{PGU}$) generated by the PGU are calculated based on its electric efficiency and fuel consumption, as shown in Eqs. (2) and (3).

$$E_{i,t}^{PGU} = \eta_i^{PGU} n_{i,t}^{PGU} \quad (2)$$

$$Q_{i,t}^{PGU} = (1 - \eta_i^{PGU}) \eta_i^{rec} n_{i,t}^{PGU} \quad (3)$$

$\eta_i^{PGU}$ and $\eta_i^{rec}$ stands for electric efficiency of the PGU and efficiency of the heat recovery unit, where both of them have been assumed as constants to simplify the calculation. The equipment efficiencies can be different for each entity $i$; however, in this work, efficiencies of the same equipment in all entities have been assumed as the same. $n_{i,t}^{PGU}$ is the amount of fuel (natural gas in this work) used by the PGU at a specific time $t$, which is a decision variable. Similar to the PGU, the boiler also generates heat by burning natural gas. The amount of natural gas used ($n_{i,t}^{bo}$) is also a decision variable.

The absorption chiller and electric chiller generate cooling by using heat and electricity, respectively. Their outputs ($C_{i,t}^{ac}$ and $C_{i,t}^{ec}$) are calculated based on the coefficient of

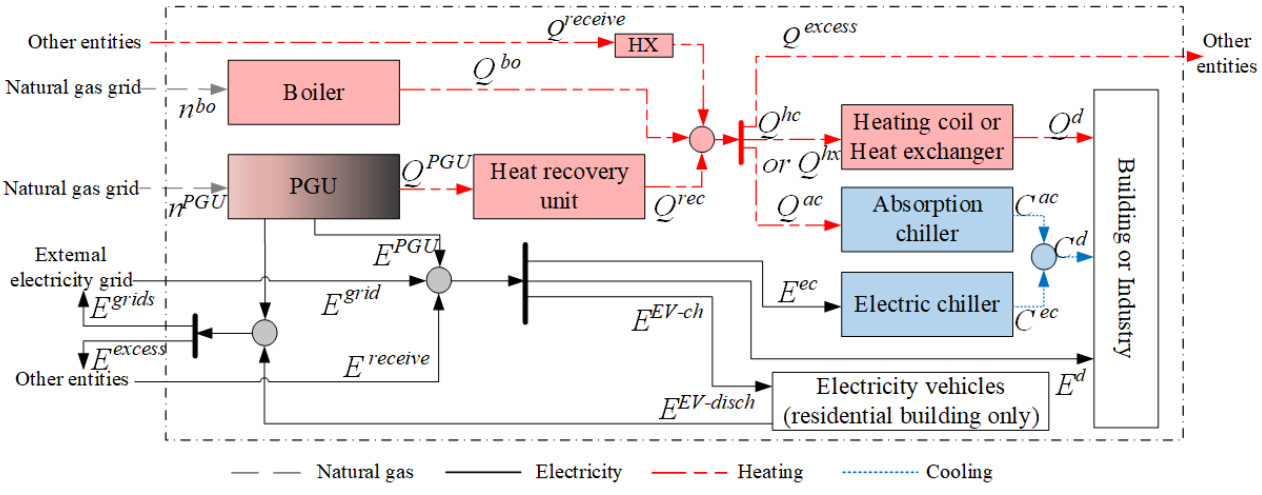


**Figure 1.** A representation of the energy system in one entity.

performance (COP) of the equipment and the decision variables – the amount of heat ($Q_{i,t}^{ac}$) and electricity ($E_{i,t}^{ec}$) used.

$$C_{i,t}^{ac} = COP_i^{ac} Q_{i,t}^{ac} \quad (4)$$

$$C_{i,t}^{ec} = COP_i^{ec} E_{i,t}^{ec} \quad (5)$$

Besides the decision variables mentioned above, the amount of electricity used to charge the EVs ($E_{i,t}^{EV-ch}$), discharge by the EVs ($E_{i,t}^{EV-disch}$), and the amount of electricity purchased from the grid ($E_{i,t}^{grid}$) are also decision variables.

Each entity in the integrated system can receive and dispatch heat and electricity to the other entities. The amount of heat ($Q_{i,i',t}^{receive}$) and electricity ($E_{i,i',t}^{receive}$) that receive by an entity $i$ from entity $i'$, as well as the amount of heat ($Q_{i,i',t}^{excess}$) and electricity ($E_{i,i',t}^{excess}$) that dispatched from entity $i$ to entity $i'$ are decision variables. In this work, it has been assumed that energy transfer, either heat or electricity transfer, between two entities at a time is in a single direction.

The decision variables mentioned above are operation decision variables that can be manipulated during the operation. The capacity of each piece of equipment ($Cap_i^{eqp}$) is the design decision variable that independent of time and cannot be modified once the system has been built. Taking the PGU as an example, the capacity and electricity output follows the relationship below:

$$E_{i,t}^{PGU} \leq Cap_i^{PGU} \quad (6)$$

## Energy balances

### Energy demands of industrial plants

Unlike the residential and commercial buildings whose energy demands are stable and are assumed as fixed profiles in this work, the energy demands of the industrial plants are adjustable by changing their production rates. The production rates of plants, $x$, are operation decision variables.

As for plants that have continuous or semi-continuous production processes, the production rate ($x_{i,t}$) represents the amount of product being generated at time $t$, which is one hour in this work. The heating, cooling, and electricity used by each process $p$ of a plant at time $t$ is calculated based on the production rate and the amount of energy required to make a unit of product ($EU_{i,p,t}^{d}$). An example of calculating the electricity demand is shown below:

$$E_{i,p,t}^{d} = x_{i,t} EU_{i,p,t}^{d} \quad (7)$$

As for plants that have batch production processes, the production rate – $x_i$ represents the amount of product being generated in a batch. Then the energy demand at time $t$ can be calculated by dividing the total energy consumption in a whole batch by the time to accomplish the process in a batch. Eq. (8) shows an example of the electricity demand. The binary decision variable $o_{i,p,t}$ is implemented to ensure each process is fully accomplished in a batch.

$$E_{i,p,t}^{d} = x_i EU_{i,p}^{d} o_{i,p,t} / TL_{i,p} \quad (8)$$

$$\sum_t o_{i,p,t} = TL_{i,p} \quad (9)$$

### Energy balances of entities

Energy balance equations are developed to ensure the energy demands of an entity can be fully satisfied. Eq. (10) shows an example of the heat balance for a residential building, where $Q_{i,i',t}^{excess}$ is the amount of heat dispatched by the residential building (entity $i$) to entity $i'$. $Q_{i,i',t}^{receive}$ represents the heat received by the residential building from other entities.

$$\frac{Q_{i,t}^{d}}{\eta_i^{hc}} + Q_{i,t}^{ac} + \sum_{i'} Q_{i,i',t}^{excess} = Q_{i,t}^{PGU} + Q_{i,t}^{bo} + \sum_i Q_{i,i',t}^{receive} \quad (10)$$

With multiple production steps, industries can require heating at different temperature levels. Therefore, instead of a single equation for the overall heat balance, like the residential building, heat balance equations for each industrial production process at a different temperature are developed for industries. It ensures the heat transfer is feasible, which is from high temperature to low temperature. $Q_{i,i',p,t}^{receive}$ represents the amount of heat received by each process from other entities.

$$\frac{Q_{i,p,t}^{d}}{\eta_{i,p}^{hc}} + Q_{i,p,t}^{ac} = Q_{i,p,t}^{PGU} + Q_{i,p,t}^{bo} + \sum_i Q_{i,i',p,t}^{receive} \quad (11)$$

Besides the individual heat balance equation for each process, an overall heat balance equation similar to Eq. (10) is also developed for the entire plant to include the amount of heat used by the absorption chiller and heat dispatched to the other entities. Since the electricity and cooling demands are not differentiated based on temperature levels, electricity and cooling balances are developed for the overall entity.

## Objective function

This work intends to find the optimal design and operation that maximize GHG emissions reduction benefits of the integrated system, measured as the GHGD%. The objective function is set as minimizing the GHG emission ratio (GHGR%) between the two systems to reduce the computation time, as shown in Eq. (12), which is equivalent to maximizing the GHGD%.

$$minGHGR\% = \min \frac{\min GHG_{int}}{\min GHG_{non-int}} \quad (12)$$

As shown in Eq. (12), minimum GHG emissions for both the integrated system and non-integrated system are necessary for calculating the GHGR%. It requires developing and solving optimization problems for both the integrated system and non-integrated system at the same time, which leads to a complex problem formulation. Alternatively, the minimum GHG emissions of the non-integrated system can be expressed as a linear equation based on the sizes of entities. The linear relationship exists because there are optimal operation patterns of equipment for the non-integrated system that does not have energy transfer among entities. When the sizes of the entities change, the optimal operation patterns remain the same, while the capacities of the equipment change correspondingly. The linear equation has been found by solving optimization problems for the non-integrated system under different entity sizes, then performing linear regressions.

# CASE STUDY DESCRIPTION

In this work, energy systems of a residential building with electric vehicles, a supermarket, a confectionery plant, a brewery, and a bakery plant have been used for case studies, as shown in Figure 2.

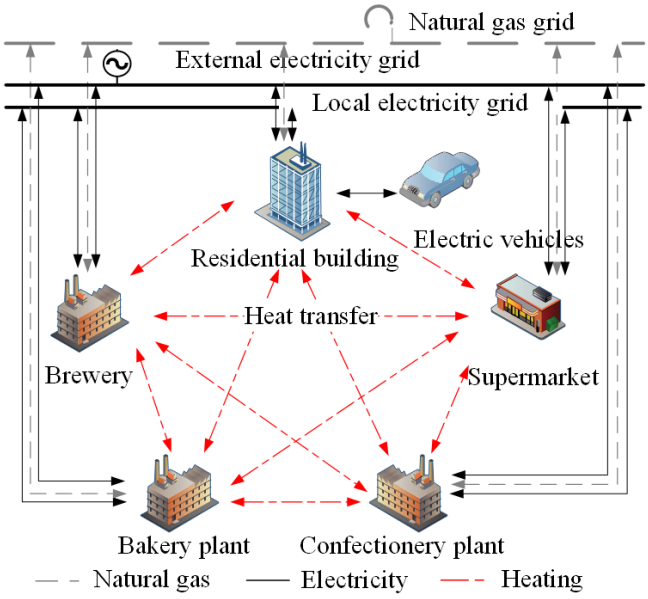


**Figure 2.** A representation of the integrated system.

Among the entities, the residential building and supermarket require more electricity than heating. Their energy demands are imported as fixed profiles, adapted based on information published by Sullivan [5] and Ghorab [6].

The confectionery plant and the brewery have higher heating demands than electricity demands, where the ratio between the heating and electricity demands of the two plants are 3.2 and 3.9, respectively. Both industries have been assumed to have continuous production processes. The bakery plant has a batch production process, which can implement electric baking ovens or gas-powered baking ovens. In this work, the gas-powered baking oven has been assumed as an indirect-fired oven, which uses heat generated by the PGU. When the baking oven is powered by electricity, the bakery plant requires more electricity than heating, where the ratio between the heating and electricity usage is 0.26. The ratio changes to 6.12 when the gas-powered baking oven is used.

In this work, case studies have been performed in both situations where the bakery plant uses electric baking ovens and the situation where gas-powered baking ovens are used. It intends to investigate the impacts of integrating entities with different energy demand patterns on GHG emissions reduction benefits of the integrated system.

## RESULTS AND DISCUSSION

### Integrated energy system with electric baking ovens in the bakery plant

Upon solving the optimization problem, it has been found that when the bakery plant uses electric baking ovens, the integrated system can achieve a maximum GHGD% of 17.5%. It requires the system to integrate 1.07 units of the residential building, 1.07 units of the supermarket, 934 electric vehicles (EVs), a brewery with a capacity of 3,934 kg/hr, and a bakery plant of 5,000 kg/day. There is no confectionery plant in the system. The 1.07 units of the residential building and supermarket stand for a residential building and a supermarket whose energy demands are 1.07 times of the ones mentioned in the Case Study Description section. The ratio between sizes of the entities is the optimal relative entity sizes that maximize GHG emission reduction of the integrated system. As shown in Figure 3, when deviating from this optimal relative entity size, the GHGD% of the integrated system becomes less than 17.5%.

Compared to the non-integrated system, the integrated system purchases 68.0% less electricity from the external grid and uses 82.5% less natural gas for operating the boiler. The reductions lead to the integrated system having lower GHG emissions compared to the non-integrated system. Additionally, the operation of the PGUs in the integrated system increased by 57.9% compared to the non-integrated system. The result indicates allowing energy transfer among entities can increase the operation of the PGUs, which reduces GHG emissions of the entire system.

In the integrated system, the brewery performs as the major electricity supplier, where 95.7% of the electricity transferred among entities is dispatched by the brewery. The electricity is sent to the residential building, bakery plant, and supermarket because the brewery requires more heating than electricity, while the three entities require more electricity than heating. Instead of operating the PGU following the lower electricity demand and using the boiler, the brewery increases the operation of the PGU to generate more heat locally. The associated excess electricity is sent to the residential building, bakery plant, and supermarket.

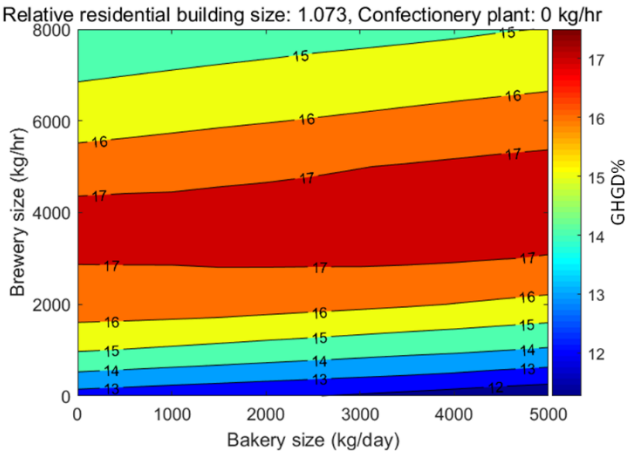


**Figure 3.** GHGD% of the integrated system where the bakery plant uses electric baking ovens.

### Integrated energy system with gas-powered baking ovens in the bakery plant

When the bakery plant uses baking ovens powered by natural gas, a maximum GHGD% of 17.6% can be achieved by the integrated system. The optimal size of the bakery plant is still 5,000 kg/day. The sizes of the residential building and supermarket slightly decrease to one unit, while the optimal capacity of the brewery is 2,812 kg/hr. Similarly, as shown in Figure 4, when deviating from the optimal relative entity size, GHGD% achieved by the integrated is less than the maximum value.

Under this system configuration, the integrated system purchases 60.8% less electricity from the grid and uses 76.1% less natural gas for operating the boilers than the non-integrated system. The operation of the PGU increases by 52.3%.

Since the bakery plant has higher heating demand than electricity demand, instead of an electricity receiver, the bakery plant becomes an electricity supplier. The amount of electricity dispatched by the bakery plant accounts for 16.8% of the total electricity transferred among entities. The brewery still performs as the major electricity supplier of the integrated system, which provides 80.6% of the total electricity transferred among entities. The electricity from both the bakery plant and brewery is transferred to the residential building and supermarket that have higher electricity demands.

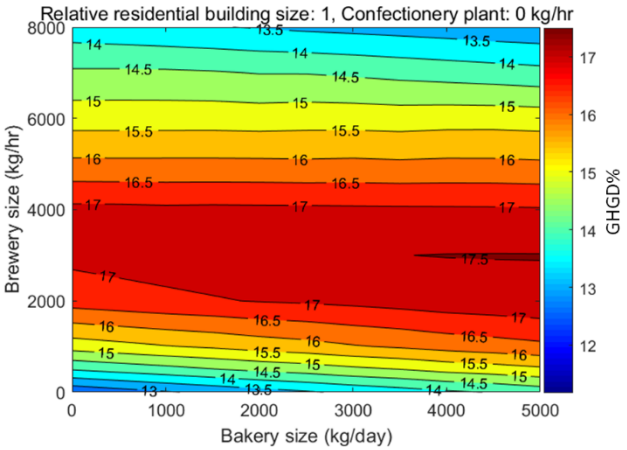


**Figure 4.** GHGD% of the integrated system where the bakery plant uses gas-powered baking ovens.

## Impacts of integrating energy systems with different energy demand patterns

Table 1 shows the highest GHGD% of the integrated system achieved under different relative sizes of the residential building. According to the results, when the relative size of the residential building increases, the highest GHGD% of the integrated system decreases. It is because there are upper bounds on the sizes of industrial plants, which limits increases of the plant sizes. Thus, the integrated system deviates from its optimal relative entity sizes and optimal operation patterns, which leads to the maximum GHGD% cannot be held.

Results in Table 1 also indicate integrating entities with different energy demand patterns leads to slightly higher GHG emissions reduction benefits of the integrated system. Under each of the relative sizes of the residential building, compared to implementing electric baking ovens, using gas-powered baking ovens in the bakery plant leads to the system having a GHGD% of 1% - 2% higher. As shown in Table 1, when the bakery plant has electric ovens that require more electricity than heating, the size of the bakery plant decreases when the size of the residential building increases. When baking ovens are powered by burning natural gas, where the bakery plant has higher heating than electricity demand, the size of the bakery plant remains at its maximum value regardless of changes in the residential building size. Under both scenarios, the sizes of the confectionery plant and brewery, which requires more heating than electricity, both increase. It is because the integrated system tends to keep a balance between the heating demand and electricity demand of the entire integrated system to avoid purchasing electricity from the grid and operating the boilers. Since the residential building requires more electricity than heating, with increases in its size, the electricity demand of the entire system also becomes greater than the heating demand. Thus, when using electric baking ovens, the size of the bakery plant decreases to avoid increasing the electricity demand of the entire system. When implementing gas-powered baking ovens, the size of the bakery plant is already at its maximum level under the optimal relative entity sizes. Therefore, when the size of the residential building increases and the entire system needs to increase its heating demand, the size of the bakery plants remains unchanged.

Overall, the results show that by optimizing the size of entities, a 15.7% - 17.6% of GHG emissions reduction can be achieved by the integrated operation. Such the GHGD% is relatively stable even when there are changes in energy demand patterns of some entities or requirements on the sizes of some specific entities that lead to the optimal entity sizes cannot be followed.

## CONCLUSION

This work quantifies the GHG emission reduction benefits that can be achieved by integrating energy systems of different sectors – residential, commercial, industrial, and transportation sectors. Even if the GHG emission of each operating energy system has been minimized by using the combined cooling, heating, and power (CCHP) system, the GHG emissions can be further reduced by transferring heat and

**Table 1:** Highest GHGD% under different relative sizes of the residential building.

| Relative size of residential building | Electric oven | | Gas-powered oven | |
|---|---|---|---|---|
| | Entity sizes | GHGD% | Entity sizes | GHGD% |
| 1 | Confectionery: 0<br>Bakery: 5,000 kg/day<br>Brewery: 4,000 kg/hr | 17.5% | Confectionery: 0<br>Bakery: 5,000 kg/day<br>Brewery: 2,812 kg/hr | 17.6% |
| 3 | Confectionery: 0<br>Bakery: 4,500 kg/day<br>Brewery: 8,000 kg/hr | 17.1% | Confectionery: 0<br>Bakery: 5,000 kg/day<br>Brewery: 8,000 kg/hr | 17.2% |
| 5 | Confectionery: 1,500 kg/hr<br>Bakery: 4,000 kg/day<br>Brewery: 8,000 kg/hr | 16.6% | Confectionery: 1,000 kg/hr<br>Bakery: 5,000 kg/day<br>Brewery: 8,000 kg/hr | 16.7% |
| 10 | Confectionery: 3,000 kg/hr<br>Bakery: 1,500 kg/day<br>Brewery: 8,000 kg/hr | 15.7% | Confectionery: 3,000 kg/hr<br>Bakery: 5,000 kg/day<br>Brewery: 8,000 kg/hr | 15.9% |

electricity among individual entities. The optimal design and operation of energy systems are determined, including the capacity and operation of equipment, the optimal production rate of plants, and the optimal relative size of entities, considering temperatures of heating demands.

Results from case studies on an integrated system with a residential building, a supermarket, a confectionery plant, a bakery plant, a brewery, and electric vehicles show the integrated operation can lead to a maximum GHG emissions reduction percentage (GHGD%) of 17.6% when the bakery plant uses gas-power baking ovens. When using electric baking ovens, the maximum achievable GHGD% is slightly lower – 17.5%.

The highest GHGD % can be maintained between 15.7% and 17.6% by optimizing the sizes of entities. Thus, even when there are requirements on sizes of specific entities and the optimal relative entity sizes cannot be followed, or there are mitigations on industrial production processes that change energy demand patterns of the entities, the integrated system still shows benefits in reducing GHG emissions than the non-integrated system.

## ACKNOWLEDGEMENTS

The authors gratefully acknowledge the financial support from McMaster Advanced Control Consortium and Ontario Research Fund.

## REFERENCES

1. Held A, Wietschel M, Pfluger B, Ragwitz M. Energy integration across electricity, heating & cooling and the transport sector–Sector coupling. *Work Pap Sustain Innov* No. S08/20:1–13 (2020)
2. Ahn H, Rim D, Pavlak GS, Freihaut JD. Uncertainty analysis of energy and economic performances of hybrid solar photovoltaic and combined cooling, heating, and power (CCHP + PV) systems using a Monte-Carlo method. *Appl Energy* 255:113753 (2019)
3. Feng L, Dai X, Mo J, Shi L. Performance assessment of CCHP systems with different cooling supply modes and operation strategies. *Energy Convers Manag* 192:188–201 (2019)
4. Fichera A, Frasca M, Volpe R. Complex networks for the integration of distributed energy systems in urban areas. *Appl Energy* 193:336–345 (2017)
5. Sullivan B. A Comparison Of Different Heating And Cooling Energy Delivery Systems And The Integrated Community Energy And Harvesting System In Heating Dominant Communities. McMaster (2020)
6. Ghorab M. Energy hubs optimization for smart energy network system to minimize economic and environmental impact at Canadian community. *Appl Therm Eng* 151:214–230 (2019)

This conference proceeding has not been peer reviewed.

CSChE Systems & Control Transactions

Open Access | Original Research

**Conference Proceedings**
Canadian Chemical Engineering Conference 2022
October 23-26, Vancouver, BC, Canada

PSEcommunity.org/LAPSE:2022.0081

PSE PRESS

# Combined Heat and Power System with Zero Carbon Emission by Integrating Catalytic Methane Pyrolysis and Carbon Conversion

**Tianyue Li[a], Jian Long[a], Wenli Du[a], Feng Qian[a]*, Vladimir Mahalec[b]***

[a] East China University of Science and Technology, Key Laboratory of Smart Manufacturing in Energy Chemical Process, Shanghai, China
[b] McMaster University, Department of Chemical Engineering, Hamilton, ON, Canada
* Corresponding Author: mahalec@mcmaster.ca.

## ABSTRACT

Many industrial plants require electricity and high temperature thermal energy which are typically generated by burning hydrocarbon fuels. This study proposes an energy system that produces electricity and thermal energy by burning hydrocarbons without emitting $CO_2$ through integration of catalytic methane pyrolysis (CMP), carbon capture and in-situ conversion (CCISC), methanol synthesis as well as combined heat and power (CHP) system. The system can eliminate $CO_2$ emissions by industrial plants and residential areas and produce methanol and carbon black as chemical by-products, in addition to producing electricity and thermal energy. Result shows that the maximum net electricity efficiency can reach 52%.

**Keywords**: Combined Heat and Power System, Methane Pyrolysis, Carbon capture and In-Situ Conversion

**Date Record:** Original manuscript received October 12, 2022. Published October 14, 2022.

## INTRODUCTION

Climate change is a global issue and has received widespread attention [1]. At present, a basic consensus has been formed on the control of greenhouse gas (GHG) emissions. Non-energy industry is an enormous part of GHG emissions, takes 31% of $CO_2$ emissions, and basic materials production has presented for approximately 22% of $CO_2$ emissions [2]. Thus, it is important to control greenhouse gas emissions by the industry. Carbon capture and utilization is an effective way to control Green House Gas (GHG) emissions. In this study, a new energy system that burns natural gas with net-zero GHG emissions has been designed and analyzed. The proposed method integrates methane pyrolysis, carbon capture in-situ conversion, combing heat and power (CHP) system, and methanol synthesis process. The system is designed to export electricity and steam to the grid which is for the residential area. Moreover, methanol and carbon black are by-products of the system which is high value and can increase the competitiveness of the system.

## BACKGROUND

### Catalytic Methane Pyrolysis

Catalytic methane pyrolysis (CMP) is a process that can convert methane into hydrogen and solid carbon without $CO_2$ emissions [3,4]. The reaction of methane pyrolysis is shown in Equation (1).

$$CH_4 \rightarrow C_{(s)} + 2H_2 \quad \Delta H_{298} = 74.8\ kJ/mol \qquad (1)$$

It works at high temperatures in the presence of metal or carbon catalyst. Methane pyrolysis is rapidly moving from the laboratory stage toward commercialization. BASF plans to use their moving bed reactor method to start large scale hydrogen production in 2030.

In the pyrolysis reactor, natural gas flow from bottom to top and carbon catalyst flow counter-current, where the heat transfer is enhanced. There are electrodes in the reactor, and the carbon is heated by the electric current and transfers heat to the natural gas.

### Carbon capture and in-situ conversion

Carbon capture and in-situ conversion (CCISC) is a laboratory level technology. It integrates Calcium-Looping (CaL) and Reverse Water Gas Shift (RWGS) in one reactor to convert $CO_2$ into CO and produce syngas as the product by $Fe_5Co_5Mg_{10}CaO$ heterojunction-redox catalysts[1] [5].

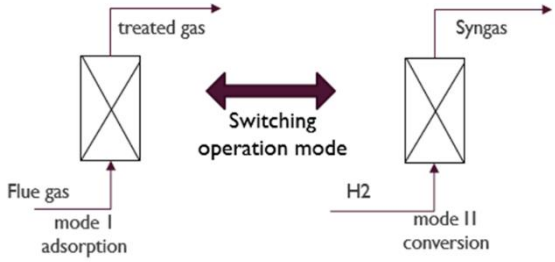


**Figure 1.** Operating modes and schematic of CaL/RWGS integrated reactor.

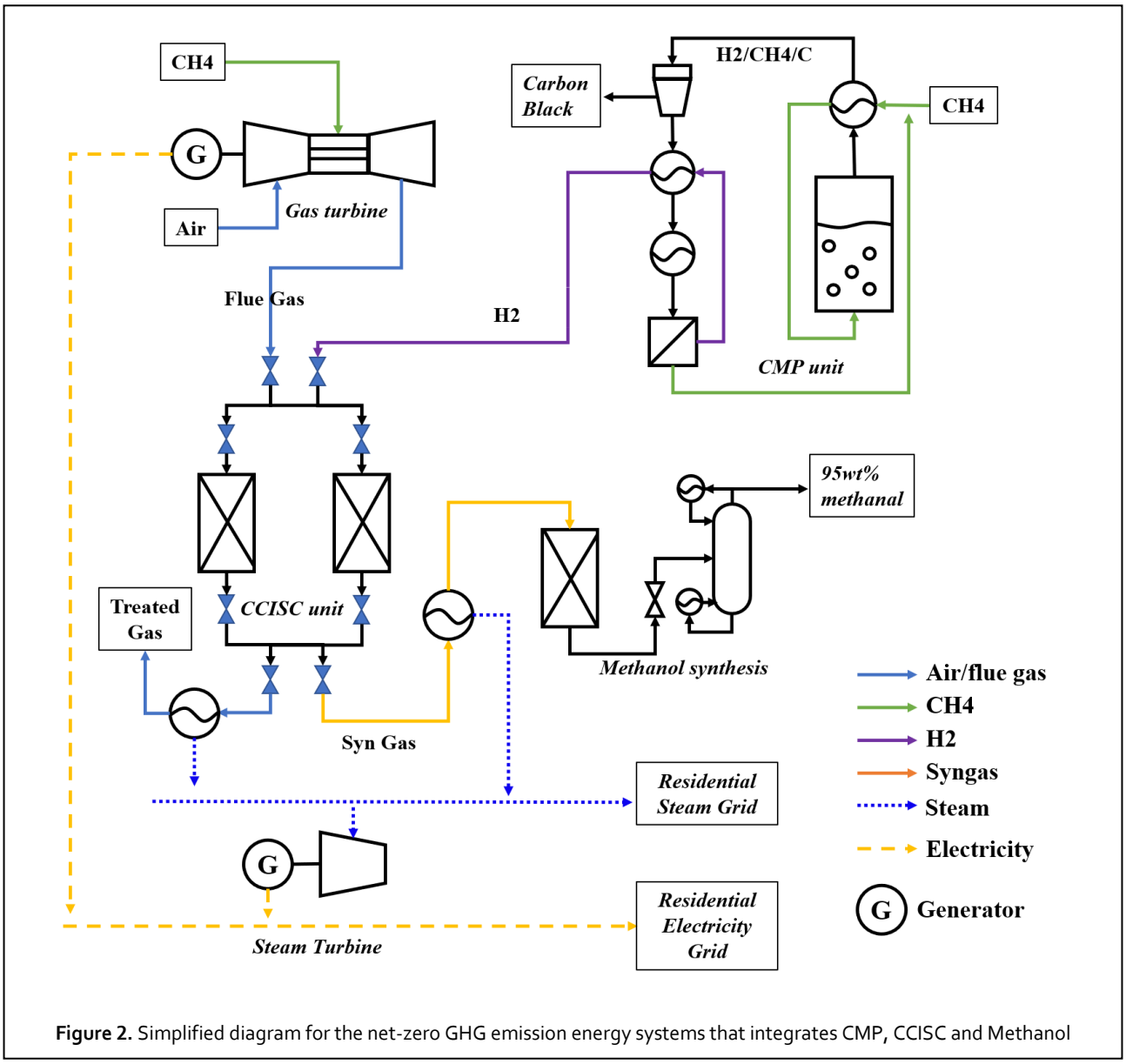


**Figure 2.** Simplified diagram for the net-zero GHG emission energy systems that integrates CMP, CCISC and Methanol

The system operates in two batch modes, as shown in Figure 1. In mode 1, the flue gas first passes through the bed where $CO_2$ is adsorbed by the catalyst and releases adsorption heat. After adsorption step, the reactor will switch from mode 1 to mode 2, the hydrogen will be added to the reactor and the reactor is heated to 650 ℃. RWGS reaction happens in mode 2, converting $CO_2$ into syngas. The reaction of RWGS is shown in Equation (2)

$$CO_2 + H_2 \rightarrow CO + H_2O_{(g)} \quad \Delta H_{298} = 41.12\ kJ/mol \quad (2)$$

Since the process requires a large amount of heat and hydrogen, a good heat integration with some heat generation process and an eco-friendly hydrogen source are required.

## PROCESS MODEL

The design of the proposed energy system is shown in Figure 2. Detailed model of the proposed system has been developed in Aspen HYSYS. The system contains five parts: Gas turbine, CMP unit, CCISC unit, Methanol synthesis and Steam turbine.

The Gas turbine is the heat source of the entire process. It produces electricity and hot flue gas; thermal energy from the flue gas is recovered in the heat recovery steam generator (HRSG). In this process, the flue first passes through the CCISC unit then through HRSG.

The CCISC unit is the key process in the system. It can remove the $CO_2$ in the flue gas of the Gas turbine by converting it into syngas which is the feedstock of the methanol synthesis. The CCISC is designed to use electricity to heat the reactor to 650°; the conversion rate can reach up to 85%.

The CMP unit is the hydrogen source of the process. This unit consumes electricity for heating. The hydrogen will be used for the CCISC unit and methanol synthesis. And the Carbon black produced by the CMP unit is valuable by-product.

The methanol synthesis process can convert syn gas into methanol, where the carbon in the syngas is converted from gas phase into liquid phase. Methanol is an important

chemical material which can produce formaldehyde, methoxy methane, olefins or alkenes.

The steam turbine is used to generate more electricity from steam generated from the HRSG. There are three kinds of steam: High pressure (HP), Medium Pressure (MP) and low pressure (LP). HP and MP will be used to generator electricity and LP will be used to the Steam grid for residential heating demand.

## RESULTS

Sensitivity analysis on Gas Turbine Fuel and Heat Output is introduced to the system.

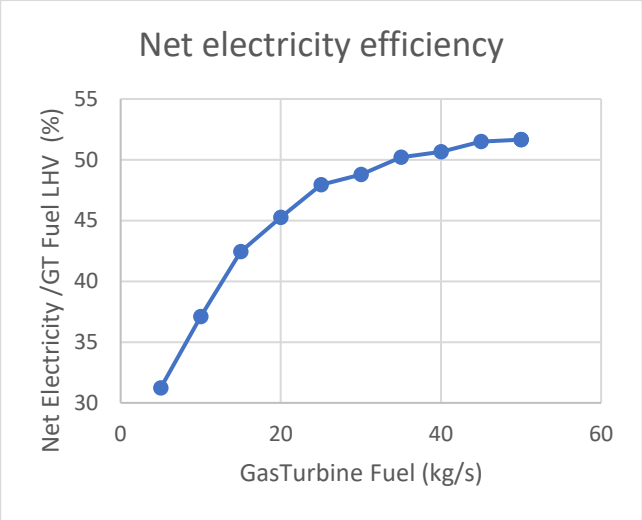


**Figure 3.** Realation between Gas Turbine Fuel and Net electricity efficiency.

As shown in Figure 3, the affect of Gas Turbine Fuel to Net electricity efficiency (Net electricity output/ Gas Turbine Fuel LHV) is tested. It is assumed there is a fixed heating demand of 100MW, and all the steam left is used to generated electricity. As GT fuel grows, the efficiency of the net electricity grows first quickly. As the GT fuel reaches 35 kg/s the efficiency will reach 50%.

As shown in Figure 4, the relation between Net electricity, Gas Turbine Fuel and Heat output is tested. The Heat output has higher impact to the Net electricity under low Gas turbine fuel.

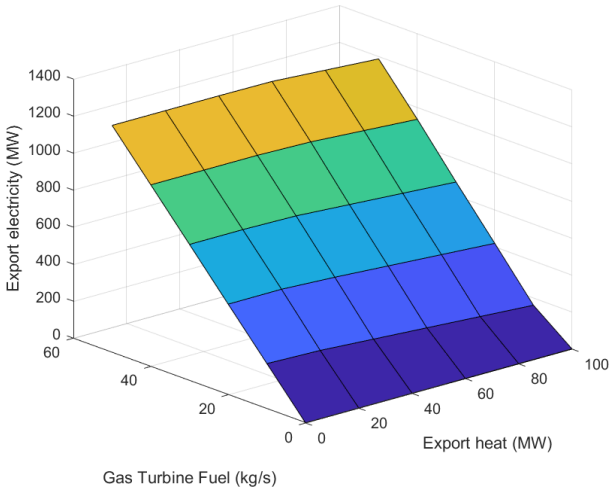


**Figure 4.** Relation between Net electricity, Gas Turbine Fuel and Heat output.

## CONCLUSIONS

This work presents a novel energy system for providing electric and thermal energy with zero carbon emission by burning natural gas. By integrating catalytic methane pyrolysis (CMP), carbon capture and in-situ conversion (CCISC), methanol synthesis as well as gas turbine combined heat and power (CHP) system, the energy system can have high energy efficiency and output carbon free electricity as well as steam for residential areas. In summary, the proposed method can eliminate GHG emission associated with production of electricity and thermal energy for residential areas and also produce methanol and carbon black. Proposed method can provide a path for reducing or completely eliminating GHG emissions produced by energy generation via burning of natural gas.

## ACKNOWLEDGEMENTS

The work has been supported by the National Natural Science Foundation of China (Basic Science Center Program: 61988101), National Natural Science Foundation of China (61725301, 61973124, 61873092), International (Regional) Cooperation and Exchange Project (61720106008). We thank McMaster University for hosting Tianyue Li from conception to completion of this work.

## REFERENCES

1. Wang, C., Geng, L. & Rodríguez-Casallas, J. D. How and when higher climate change risk perception promotes less climate change inaction. *J. Clean. Prod.* 321:128952 (2021)
2. Wang, H. & Chen, W. Modelling deep decarbonization of industrial energy consumption under 2-degree target: Comparing China, India and Western Europe. *Appl. Energy* 238:1563–1572 (2019)
3. Sánchez-Bastardo, N., Schlögl, R. & Ruland, H. Methane Pyrolysis for Zero-Emission Hydrogen Production: A Potential Bridge Technology from Fossil Fuels to a

Renewable and Sustainable Hydrogen Economy. *Ind. Eng. Chem. Res.* 60:11855–11881 (2021)
4. Abbas, H. F. & Wan Daud, W. M. A. Hydrogen production by methane decomposition: A review. *Int. J. Hydrog. Energy* 35:1160–1190 (2010)
5. Shao, B. et al. Heterojunction-Redox Catalysts of Fex-CoyMg10CaO for High-Temperature $CO_2$ Capture and In-situ Conversion in the Context of Green Manufacturing. Energy Environ. Sci. 14:2291–2301 (2021).

This conference proceeding has not been peer reviewed.



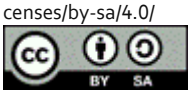

CSChE Systems & Control Transactions

Open Access | Original Research

**Conference Proceedings**
Canadian Chemical Engineering Conference 2022
October 23-26, Vancouver, BC, Canada

PSEcommunity.org/LAPSE:2022.0088

PSE PRESS

# Interactions between process design and process control: Passive cooling in a micro refinery process

**Mahdi Sharifian[a], Nicolas Hudon[b], Gregory S. Patience[a]***

[a] Polytechnique Montreal, Department of chemical engineering, Montreal, Quebec, Canada
[b] Department of chemical engineering, Queens University, Kingston, ON
* Corresponding Author: Gregory-s.patience@polymtl.ca

## ABSTRACT

A micro refinery unit at Polytechnique Montreal converts natural gas to diesel range fuel as the main product in two high pressure and high temperature reacting units. First, it transforms methane to syngas by catalytic partial oxidation (CPOX) at 20 bar and 800°C. Then, it produces the medium-chain hydrocarbons from syngas by Fischer-Tropsch (FT) reaction at 20 bar and 300°C.

The aim of this study is to evaluate the impact of passive intercooling on the performance and robustness of a pre-set control configuration for this sequence of interconnected chemical reactors. We simulate the whole process in Aspen Plus v8.4 and first design a PI temperature controller for the Fischer-Tropsch reactor in Aspen Plus Dynamics. As the FT process is highly exothermic, the controller is essential to properly remove the heat generated in the reactor. Despite being feasible in simulations, the closed-loop results suffer from many shortcomings, notably with respect to process constraints.

The impact of intercooling on the closed-loop dynamics is studied by decoupling thermally the reactors using a passive intercooler to remove the excess heat from the syngas at the exit of the CPOX reactor.

Simulation results show that intercooling improves the performance of the FT operation and reduces the control cost as it keeps the control system far from the cooling flow constraints in the FT reactor. In this case, the controller has an acceptable performance against the step changes in temperature and has a built-in robustness against underestimated heat exchange within the FT process.

**Keywords**: Process control, micro refinery, passive cooling

**Date Record:** Original manuscript received October 14, 2022. Published October 19, 2022.

## INTRODUCTION

The energy demand is growing dramatically as the world's population keeps on increasing and economies proceed [1]. Since the capacity of the exploitable oil is decreasing, other virgin resources such as associated and stranded gas reservoirs are notably marked [2]. Among these options, Gas-to-Liquid (GtL) processes have the potential to transform the natural gas or associated gas into the higher-value hydrocarbons as synthetic fuel. In particular, the liquid synthetic fuels are promising alternatives of oil-related transportation sector since the price of crude oil gradually rises while its reservoirs are going to finish [3]. However, large scale industrial GTL plants are not always economical as in most cases, building a commercial plant needs a huge investment resulting in the plant to be infeasible. Moreover, in some areas, providing the industrial utilities such as water resource and electricity is limited or sometimes impossible.

In such cases, to exploit the gas reservoir and convert it to the added value fuels, micro-scale GTL process which is called Micro Refinery Unit (MRU) is feasible as it needs a lesser investment and consume much lower utility as well. The FT reaction is highly exothermic [4, 5] and one of the main challenges of such reactions is having a safe and accurate start up and to provide a stable operation [6]. Among research on the reactor design and configuration to improve the heat removal from FT process, a few studies focused on the design of temperature controller [7]. An appropriate feedback control throughout the process is essential to prevent runaway reaction which causes catalyst deactivation, loss of selectivity and conversion and/or loss of operability that can induce the reactor explosion [8, 9].

In this paper, we first describe the overall CPOX/FT process. We first consider PI control for the temperature of the FT reactor. We then consider the combination of passive cooling and PI control to regulate the temperature of the FT reactor. Finally, we study via simulations the impact of heat exchange uncertainty on the closed-loop dynamics.

## PROCESS OVERVIEW AND CHALLENGE

The process consists of thermal-sustained catalytic partial oxidation (CPOX) at 800⁰C and 20 bar to convert the natural gas into syngas (H2 and CO) and Fischer-Tropsch reaction (FT) at 300⁰C to produce diesel from syngas on Iron-based catalyst. The FT reactor is a coiled fluidized bed. To remove the generated heat and adjust the temperature of FT reactor, a control system is considered to manipulate the cooling water flow through the coil. Two challenges in the design of FT section are:

- To decrease the temperature of the syngas from CPOX to FT reactor.
- To improve the performance of the temperature controller against the disturbances in the syngas feed to the FT reactor.

Hence, we develop a simulation-based controller design by Aspen Plus Dynamic v8.4 in two scenarios; with a passive intercooler between the reactors and without it and then compare the results of FT temperature to complete the design based on the efficient method.

## PROCESS CONTROL

### Modeling and simulation

We first solve the gas to liquid (GtL) process in steady state. A Gibbs reactor resembles the CPOX by considering all the possible components in the product. To simulate the fluidized bed FT reactor, we applied a CSTR and attached a Longmuir-Hishelwood-Hougen-Watson (LHHW) kinetics [10] which is adopted to the experimental data of RIPI for the commercialized iron-based catalyst [11, 12]. Thus, the governing stoichiometry and kinetics for the Fischer-Tropsch and water gas shift (WGS) reactions are:

$$\mathrm{FT}: \ 9\mathrm{CO} + 19\mathrm{H_2} \ \rightarrow \mathrm{C_9H_{20}}\ (\mathrm{C^*}) + 9\mathrm{H_2O} \tag{1}$$

$$\mathrm{WGS}: \mathrm{CO} + \mathrm{H_2O} \ \rightarrow \mathrm{CO_2} + \mathrm{H_2} \tag{2}$$

$$r_{FT} = K_{FT}\frac{P_{H_2}P_{CO}}{P_{CO} + a_{FT}P_{H_2O} + b_{FT}P_{CO}} \tag{3}$$

$$r_W = K_W\frac{P_{CO}P_{H2O} - \frac{P_{H_2}P_{CO_2}}{K_P}}{P_{CO} + a_wP_{H_2O} + b_wP_{CO_2}} \tag{4}$$

$$K_i = k_i^{\circ}\, exp\left(-\frac{E_i}{RT}\right) \tag{5}$$

$$ln(K_P) = \frac{4578}{T} - 4.33 \tag{6}$$

$C^*$ is the mixture of hydrocarbons in the product stream based on [12]. Table (1) shows the parameters of the equations (3) to (6).

**Table 1**. Kinetic parameters of FTs

| Parameter | Value | Unit |
|---|---|---|
| $k_{FT}^{\circ}$ | $2.1 \times 10^{-3}$ | kmol/(kg. s. Pa) |
| $E_{FT}$ | 86 | $kJmol^{-1}$ |
| $a_{FT}$ | $1.25 \times 10^{-7}$ | $Pa^{-1}$ |
| $b_{FT}$ | $7 \times 10^{-6}$ | $Pa^{-1}$ |
| $k_W^{\circ}$ | 1079.4 | kmol/(kg. s. Pa) |
| $E_W$ | 132 | $kJmol^{-1}$ |
| $a_w$ | $2.78 \times 10^{-6}$ | $Pa^{-1}$ |
| $b_w$ | $1.23 \times 10^{-5}$ | $Pa^{-1}$ |

The intercooler cools down the syngas stream from 800⁰C to 300⁰C which is the operating temperature of fluidized bed FT reactor. Table 2 summarizes the characteristics of the MRU.

**Table 2**. Specifications of the FT reactor

| Spec | Value |
|---|---|
| FT reactor dimensions (mm) | $200 \times 1600$ |
| Coil diameter (in.) | 3/4 |
| Coil length (m) | 12 |
| Density of the Iron catalyst ($kg/m^3$) | 1290 |
| Bed porosity | 0.6 |
| Catalyst diameter (m) | $2 \times 10^{-4}$ |
| Air flow (mole/h) | 1190 |
| Natural gas flow (mole/h) | 500 |

Equations (7, 8) determine the heat transfer coefficient as well as inlet and outlet temperature of cooling water through the internal coil of FT reactor.

$$Q = UA\Delta T_{LM} = \dot{m}_c\left(T_{c,o} - T_{c,i}\right) \tag{7}$$

$$\Delta T_{LM} = \frac{\left(T_b - T_{c,i}\right) - \left(T_b - T_{c,o}\right)}{\ln\left(\frac{T_b - T_{c,i}}{T_b - T_{c,o}}\right)} \tag{8}$$

The resulted values for $T_{c,i}$ and $T_{c,O}$ as well as liquid holdup of the coil required for the dynamic simulation are filled in the dynamic sheet of the CSTR in Aspen Plus.
Next, we switch to the pressure driven mode and export the simulation to the dynamic module.

### Control strategy

A temperature control module is attached to the reactor based on the "heating medium flow" as the process variable. Then, we applied the internal model control technique to tune the parameters of a PI controller [13]. Figure (1) represents the process flow diagram in the dynamic mode.

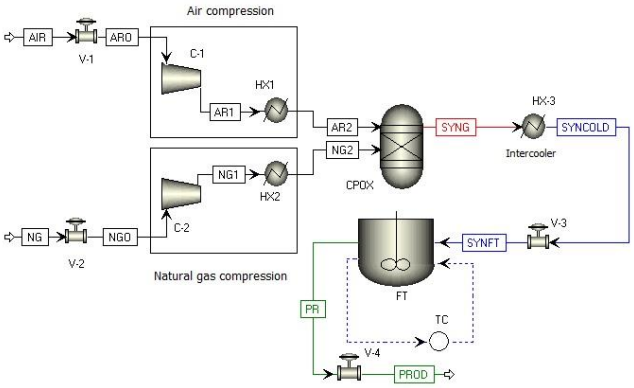


**Figure 1.** Process flow of MRU in Aspen Plus Dynamics V8.4

## RESULTS AND DISCUSSION

Steady-state simulation and heat transfer functions determine the characterizations of the cooling coil (Table 3).

**Table 3.** Computed parameters of FT for the dynamic simulation

| Spec | Value |
|---|---|
| $Q_{FT}$ , $kW$ | 12.3 |
| $\dot{m}_c, kgh^{-1}$ | 540 |
| $UA, WK^{-1}$ | 167 |
| $T_{c,i}$, ℃ | 208 |
| $T_{c,o}$, ℃ | 226 |
| $T_{app}$, ℃ | 74 |

In the dynamic mode, a step change in the output variable (cooling flow rate) in the open loop determines the parameters of the PI controller (Figure 2).

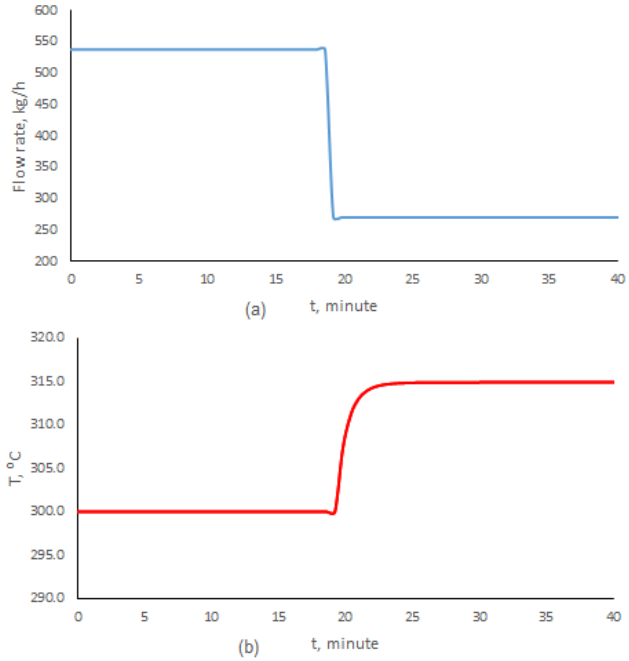


**Figure 2.** Open-loop response of the FT temperature, (a) step change in coolant flow rate, (b) temperature response.

Thus, the transfer function of the FT process is:

$$G(s) = \frac{0.06e^{-0.005s}}{0.92s + 1} \tag{9}$$

And the parameters of the PI controller are $K_c = 18.1$ and $\tau_I = 0.92\ minute$.

### Control without passive cooling

To investigate the impact of passive cooling system, first we removed the intercooler by putting the duty of HX3 equal to 0 in the dynamic simulation meaning no change in the temperature of syngas to FT reactor (800°C). In this case, the simulation shows that the control system of FT fails to recover the desirable temperature of FT process (Figure 3).

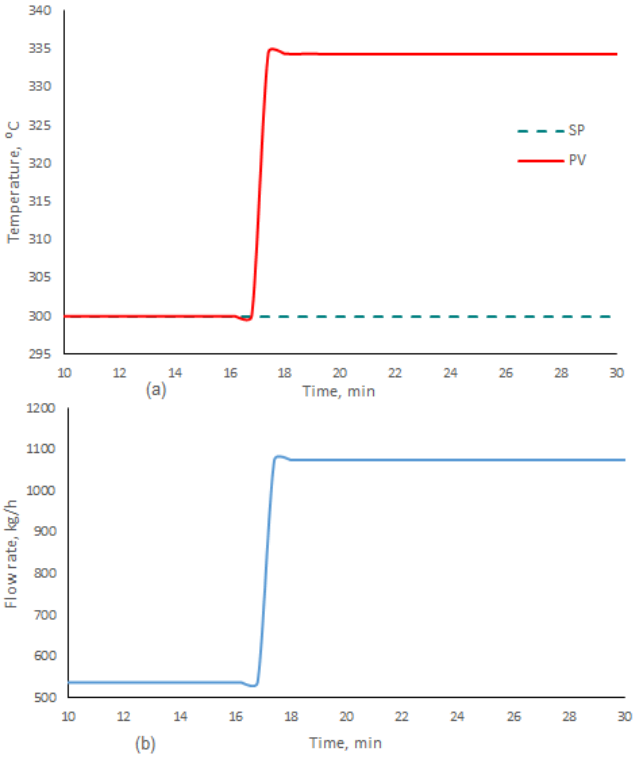


**Figure 3.** Response of the temperature controller in case of no passive cooling, (a) FT temperature and set point, (b) coolant flow rate. SP is setpoint and PV is the process variable.

Therefore, designing the process without passive cooling not only damage the catalyst, also cause a control failure and reaction run away.

### Control with passive cooling

In this case, we keep the intercooler, HX3 (Figure 1) between the reactors to decrease the syngas temperature and make it close to the operating temperature of the FT reactor (300°C). However, HX3 has no automatic temperature control and the coolant flow rate is adjusted in the start-up by a manual valve.

#### Step change in the set point

The response of the FT temperature against ±5°C in the set point confirms that the controller has an appropriate performance in case of involving the passive cooling (Figure 4).

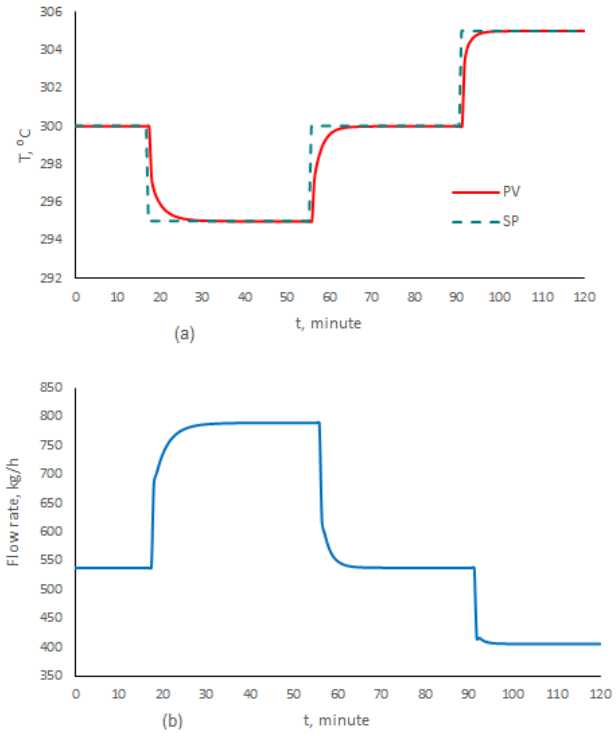


**Figure 4**. Closed loop response of the FT temperature by ±5°C in set point, (a) temperature variation, (b) coolant flow rate as the control output

## Disturbance in the syngas temperature

The temperature of the syngas entering the FT reactor may changes due to an upstream variation or insufficient heat transfer across the intercooler. We simulate this case by decreasing the heat duty of HX3 by 10% which rises the temperature of SYNFT from 300°C to 350°C (Figure 1). The results show that the controller properly recovers the set temperature inside the FT reactor (Figure 5).

It also reconfirms the positive impact of the passive cooling in the design of MRU. Although the intercooler may not perfectly cool down the syngas stream up to the operating temperature of the FT, it assists the temperature controller to adjust the temperature and concentrations in FT reactor.

## Robustness of the controller

One challenge in the modeling and simulation of the FT synthesis as an exothermic process is the uncertainty of the overall heat transfer coefficient (U) since the real value is higher than what is obtained from the correlations [14].

We increased the UA as the manipulated variable in Aspen dynamics by 10%. According to the results, the controller is capable to adjust the temperature on its set point if U is underestimated (Figure 6).

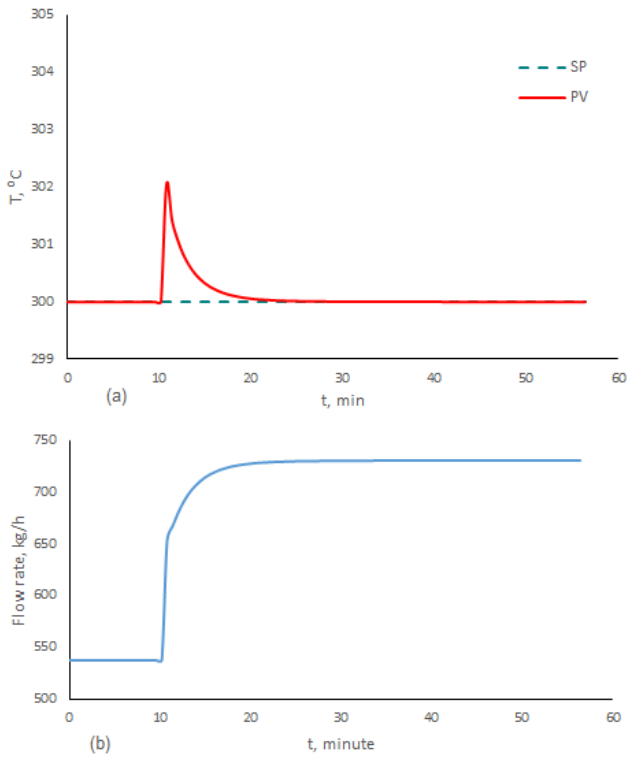


**Figure 5**. Closed loop response of the FT temperature in case of 10% thermal inefficiency of the intercooler, (a) temperature and set point in FT, (b) coolant flow rate as the control output.

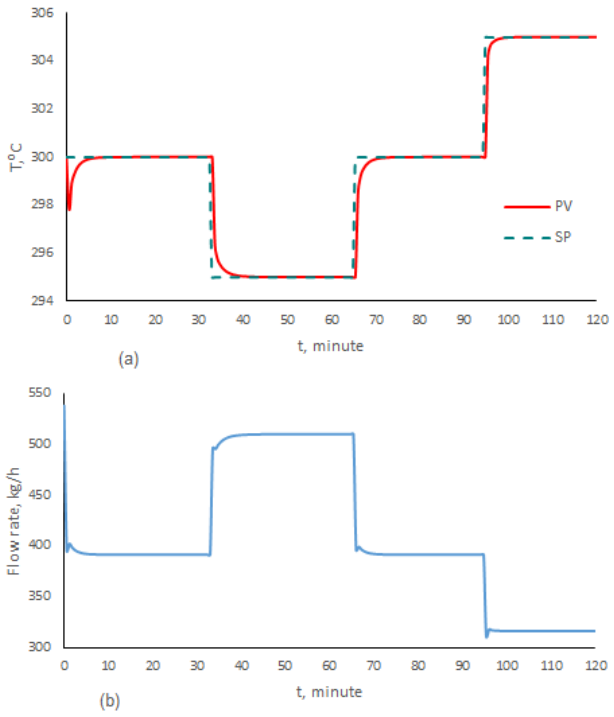


**Figure 6**. Robustness of the temperature controller against 10% increase in overall heat transfer coefficient between the cooling coil and the reactor, (a) FT temperature, (b) coolant flow rate

## CONCLUSION

A micro refinery process was simulated by Aspen plus dynamics v8.4. This process consists of CPOX and FT both of which are exothermic reactions. Thus, the designing a proper cooling system improves the operability and efficiency of the process. In the conceptual design, we considered a passive intercooler between the two reactors to cool down the syngas stream into the operating temperature of the iron catalyzed FT reaction. The CPOX is simulated by a Gibbs reactor and the FT reactor is simulated by a CSTR. For the FT process, we combine a practical LHHW kinetic model with heat transfer between the internal cooling coil and the fluidized bed of FT reactor. Then we design a PI temperature controller based on the dynamic behavior of FT to remove the generated heat inside the reactor. The results show that involving a passive intercooler improves operability of the FT reactor, prevent reaction runaway, and gently decreases the thermal shocks through the reactor. In addition, the control system is robust in case of underestimation of overall heat transfer coefficient and is capable to recover the temperature of FT reactor against the step change in the set point and disturbances in the temperature of the feeding syngas to FT reactor. It is notable that the controller needs to change the cooling water flow rate so much just to change a few on the temperature which mainly refers to the strong exothermic nature of the FT reaction. Hence, other cooling alternative such as evaporative cooling might be more appropriate.

## ACKNOWLEDGEMENTS

This project is supported by Canada research chair in high temperature, high pressure heterogeneous catalysis.

## REFERENCES

1. Wood DA, Nwaoha C, Towler BF. Gas-to-liquids (GTL): A review of an industry offering several routes for monetizing natural gas. *J. Nat. Gas Eng.* 9:196–208 (2012).
2. Ostadi M, Dalane K, Rytter E, Hillestad M. Conceptual design of an autonomous once-through gas-to-liquid process—Comparison between fixed bed and microchannel reactors. *Fuel process. technol.* 139: 186–195 (2015).
3. Sudiro M, Bertucco A. Production of synthetic gasoline and diesel fuel by alternative processes using natural gas and coal: Process simulation an optimization. *Energy*. 34(12):2206–2214 (2009).
4. Zhang X, Qian W, Zhang H, Sun Q, Ying W. Effect of the operation parameters on the Fischer–Tropsch synthesis in fluidized bed reactors. *Chin. J. Chem. Eng.* 26(2):245–251 (2018).
5. Rafiq MH, Jakobsen HA, Schmi R, Hustad JE. Experimental studies and modeling of a fixed bed reactor for Fischer–Tropsch synthesis using biosyngas. *Fuel process. technol.* 92(5):893–907 (2011).
6. Haugwitz S, Hagander P. Challenges in start-up control of a heat exchange reactor with exothermic reactions; a hybrid Approach. *IFAC Proc. Volumes*. 39(5):185–190 (2006).
7. Méndez CI, Ancheyta J. Modeling and control of a Fischer-Tropsch synthesis fixed-bed reactor with a novel mechanistic kinetic approach. *J. Chem. Eng.* 390:124489 (2020).
8. Caetano R, Lemos MA, Lemos F, Freire F. Modeling and control of an exothermal reaction. *J. Chem. Eng.* 238:93-99 (2014).
9. Schweitzer JM, López-García C, Ferré D. Thermal runaway analysis of a three-phase reactor for LCO hydrotreatment. *Chem. Eng. Sci.* 65(1):313–321 (2010).
10. Zimmerman WH, Bukur DB. Reaction kinetics over iron catalysts used for the fischer-tropsch synthesis. *Can. J. Chem. Eng.* 68(2):292–301 (1990).
11. Marvast MA, Sohrabi M, Zarrinpashne S, Baghmisheh G. Fischer-Tropsch Synthesis: Modeling and performance study for Fe-HZSM5 bifunctional catalyst. *Chem. Eng. Technol.: Industrial Chemistry-Plant Equipment-Process Engineering-Biotechnology*. 28(1):78–86 (2005).
12. Rahmati M, Mehdi M, Bargah Soleimani M. Rate equations for the Fischer-Tropsch reaction on a promoted iron catalyst. *Can. J. Chem. Eng.* 79(5):800–804 (2001).
13. Seborg DE, Edgar TF, Mellichamp DA, Doyle III FJ. Process dynamics and control. John Wiley & Sons, 2016.
14. Zhang Y, Wei Q. CPFD simulation of bed-to wall heat transfer in a gas-solids bubbling fluidized bed with an immersed vertical tube. *Chem. Eng. Process.: Process Intensification*. 116:17–28 (2017).

This conference proceeding has not been peer reviewed.



CSChE Systems & Control Transactions

Open Access | Original Research

**Conference Proceedings**
Canadian Chemical Engineering Conference 2022
October 23-26, Vancouver, BC, Canada

PSEcommunity.org/LAPSE:2022.0089

PSE PRESS

# Deep Chemometrics using One Dimensional Convolutional Neural Networks for Predicting Crude Oil Properties from FTIR Spectral Data

**Souvik Ta[a], Shahla Alizadeh[a], Lakshminarayanan Samavedham[a,b] and Ajay K. Ray[a*]**

[a] Department of Chemical and Biochemical Engineering, Western University, Canada N6A 5B9
[b] Department of Chemical and Biomolecular Engineering, National University of Singapore, Singapore
* Corresponding Author: aray@eng.uwo.ca

## ABSTRACT

The determination of physicochemical properties of crude oils is a very important and time-intensive process that needs elaborate laboratory procedures. Over the last few decades, several correlations have been developed to estimate these properties, but they have been very limited in their scope and range. In recent years, methods based on spectral data analysis have been shown to be very promising in characterising petroleum crude. In this work, the physicochemical properties of crude oils using FTIR spectrums are predicted. A total of 107 samples of FTIR spectral data consisting of 6840 wavenumbers is used. One Dimensional convolutional neural networks (CNNs) were used with FTIR spectral data as the one-dimensional input and Keras and TensorFlow were used for model building. The Root Mean Square Error decreased from 160 to around 60 for viscosity when compared to previous machine learning methods like PLS, PCR, and PLS-GA on the same data. The important hyper-parameters of the CNN were optimised. In addition, a comparison of results obtained with different neural network architectures is presented. Some common preprocessing techniques were also tested on the spectral data to determine their impact on model performance. To increase interpretability, the intermediate neural network layers were analysed to reveal what the convolutions represented, and sensitivity analysis was done to gather key insights into which wavenumbers were the most important for prediction of the crude oil properties using the neural network.

**Keywords**: FTIR, Crude Oil Properties, Neural Network architectures, One Dimensional Convolutional Neural Network

**Date Record:** Original manuscript received October 15, 2022. Published October 19, 2022.

## INTRODUCTION

Determination of crude oil properties and its characterization has long been one of the most important preliminary/critical steps for different aspects of oil refinery and reservoir calculations. Crude oil viscosity is one of the properties that determines how the crude flows in the system and hence is important to determine along with others like sulfur percentage and the cuts of other crudes. These properties are generally determined by laboratory experimentation; the related methods have evolved for years. Traditionally, the characterization of crude oil has been carried out using various chromatography methods, but these are intensive, expensive and time-consuming. The separation and identification of two or more major components could take a year or more using classical analytical methods [1]. Gas Chromatography and its combination with GC-MS has been very instrumental in analyzing petroleum components [2]. GC has been used to evaluate reservoir compartmentalization and connectivity [3]. However, these methods are extensively time and resource consuming and involve a lot of sample preparation and testing.

As an alternative, Fourier transform infrared spectroscopy technique (FTIR) has been deployed to characterize crudes. Abdulkadir et al. [1] determined that IR spectroscopy is indeed viable for characterizing crude oils and models can be using Partial Least Squares (PLS) regression on FTIR data. They used it to predict the aliphatic content and saturates for 5-7 samples. Brito et al. [4] have used human-saliva FTIR spectra coupled with support vector machines (SVMs) to find the best wavenumber regions to predict blood glucose levels.

Earlier, Principal Component Regression (PCR) on the preprocessed FTIR Spectra was used to predict density and viscosity with very good results for density and acceptable results for viscosity [5]. However, to improve the performance of the previous machine learning methods further a model with neural networks is attempted. Since fairly good performance with the PLS and PCR regression models were achieved earlier, an artificial neural network (ANN) would not provide much of a performance increase. Recently, some literature has shown

that one dimensional CNNs can be used to take spectral information as input generating good predictions of different properties [6-9] in soil, plant leaves, pharmaceutical tablets etc.

## METHODOLOGY

### Dataset

The crude oil samples used in this study were obtained from seven different Canadian oil fields provided by an energy corporation company in Canada. The FTIR spectral information corresponding to these samples were obtained using a Thermo Fisher Scientific FTIR microscope. Other physicochemical properties crucial to the characterization of crude were obtained using appropriate analytical instruments and laboratory methods by the company was provided. Overall, 107 samples of crude with 6366 wavenumbers each are used as attributes. The output space had 13 properties with most important being density and viscosity. Other properties included sulphur content, Total Acid Number, Micro Carbon Residue and the yields of different cuts of the crude.

### Dataset Analysis and Preprocessing

Upon analyzing the correlation of output space attributes, it was found that most of them were highly correlated with density or viscosity. In our previous paper [5], both density and viscosity were predicted using machine learning methods; particularly good predictions were obtained for density using PCR, but the error for viscosity was not within acceptable limits. Hence, the more advanced CNN architecture for predicting the viscosity was investigated. The data was cleaned by removing the first 476 wavenumbers from the spectra due to missing values and noise. The resulting data was subject to auto-scaling so that all variables (spectral values at each wavenumber) have mean equal to zero and standard deviation equal to one.

### Convolutional Neural Networks

CNN is a widely used class of deep learning architectures primarily used in computer vision applications. Recent studies have started to use a modified CNN called a one-dimensional CNN to predict properties from spectral information [6-9]. In these applications, the spectral information is regarded as a one-dimensional image and fed to the input layer. CNNs are generally made up of three types of layers: convolutional layers, pooling layers and fully connected layers and a network is created by stacking them [10].

#### Convolutional Layer

The convolutional layer is the most vital layer in a CNN and uses learnable kernels to train. The filters in a convolutional layer convolve over the entire input to generate a 2D activation map [10, 11]. The network then learns the values in the kernel to fire when a specific feature is detected. These layers can decrease the complexity and number of parameters compared to a traditional ANN. The common hyper-parameters for this layer are depth, stride and zero-padding. Depth is the depth of the output or the number of kernels; Stride is the number of pixels the filters move by when convolving on the input. Increasing stride can result in less overlap and reduce the output dimensions but it can also capture less data. Zero-padding is used to pad the border of the input with zeros and hence preserve the data near the corners and also the dimensions.

To calculate the output dimensions of the convolutional layer, the formula used is Output Size = 1+ (N-F)/S

where N is Input Size, F is Filter Size and S is Stride,

#### Pooling layer

Pooling layers are used to reduce the dimensions of the layers which further reduces the number of parameters and the computational complexity, The most common kind of pooling is max pooling which replaces the value of a kernel with the MAX value inside it [11]. The most common filters used for max pooling are 2*2 with a stride of 2. This doesn't cause any overlap of filters. Generally, increasing the kernel size causes a loss in information and decreases performance greatly [10].

#### Fully Connected Layer

A fully connected layer is very similar to how neurons are connected in a traditional ANN in which each neuron in one layer is connected to each neuron in the next layer. This generally results in a lot of trainable parameters and is generally used to connect the features from the convolutions to the output [10, 11].

#### Common architectures

The CNN's generally follow a common architecture in which one cant just connect any type of layer after another. Generally convolutional layers are stacked with pooling layers and this forms an unit of a convolutional layer and a pooling layer which is repeated and is finished with a fully connected layer. Sometimes stacking two convolutional layers followed by a pooling layer to form an unit helps in selecting more complex features [10].

#### Gaussian Noise

A Gaussian noise layer was used with a standard deviation of 0.05. This layer adds noise with a mean of zero and a specified standard deviation to the input layer. Studies [12] suggest adding Gaussian Noise can have a regularizing effect and reduce overfitting.

#### Dropout Layer

Dropout randomly drops nodes from the layer while training and simulates the effect of ensemble learning. In this work, a dropout layer was used to add a regularizing effect and prevent overfitting. The amount of dropout to use will be investigated as a hyperparameter [13].

### One Dimensional CNNs

One dimensional CNNs are a modified version of the conventional deep CNNs and use only an one dimensional input of the shape [n,1]. 1-D CNNs have shown some advantages over the deeper traditional CNNs [14]. They require simple array operations as opposed to more bulky matrix operations in CNNs; this significantly reduces the computational load. Studies have shown that 1D CNNs are really good at performing signal processing tasks with a relatively shallower architecture which is easier to train and implement. Since we are using this in an industrial setting, 1D CNNs having a much lower computational load helps in implementing it as a more cost effective and real time solution.

1D CNNs have been used in a lot of signal processing applications including those that involve ECGs signal and vibration data[14]. In recent studies, 1D CNNs have been proved to work very well with spectral information as an input

– this enabled gaining insights and useful predictions from data. There have been applications in soil quality predictions [6, 7]. Kawamura et al. [7] have used it on Vis-NIR spectra to estimate available phosphorus in soil. Ng et al. [6] have also used spectral information from combined sources like Vis-NIR and MIR to predict several soil properties. Prilianti et al. [8] have successfully used a 1D CNN to predict pigment concentration in leafs from the reflectance spectra. Bjerrum et al. [9]have developed methods like data augmentation and scatter correction specially for 1DCNNs and successfully predicted drug content in tablets from NIR spectra. However, there is lack of literature that describes the use of 1D CNNs in petrochemistry with FTIR spectra and this is the matter of investigation in this study.

### Hyperparameters

The most important hyperparameters to be tuned were the batch size, learning rate and the optimization technique employed. All models were trained with epochs around 200-300 with early stopping and reduceLRonPlateau callbacks.

**Table 1:** Initial Hyperparameter Search Space

| Hyperparameter | Search Space |
|---|---|
| Batch size | 8,16,32,64 |
| Epochs | 150-300 |
| Learning Rate | 0.01,0.001 |

We tested seven different gradient descent-based optimization techniques to train our algorithms. They are Stochastic Gradient Descent, Adagrad, Adadelta, RMSProp, Adam, Adamax and Nadam [15].

### Neural Network Architecture

Previous studies of using 1D CNNs on spectra suggest that shallow networks perform much better than deep networks and hence we decided to go forth with shallow networks for our models. This also helps us with the reduced computational load and aids realtime application[8]. For the initial testing of hyperparameters, a standard 2 hidden layer CNN was used alongwith Gaussian Noise and Dropout. The architecture is shown in Table 2.

**Table 2**: Architecture of 1D CNN used for hyperparameter testing.

| Layer | Parameters |
|---|---|
| Gaussian Noise | Standard deviation = 0.05 |
| Conv 1D | no of filters = 32; kernel size = 8; ReLU |
| Conv 1D | no of filters = 32; kernel size = 16; ReLU |
| Dropout | dropout = 0.5 |
| Dense Layer | no of units = 128; ReLU |
| Dense Layer | no of units = 1; Linear |

After the initial hyperparameters were determined, the best batch size and learning rate were fixed to decide the best neural network architecture for our data. For this, a Neural Architecture Search approach was implemented using kerastuner in Tensorflow [16]. Neural Architecture Search is automated architecture engineering algorithm which determines the best neural network architecture. Generally, it has three dimensions: Search Space, Search Strategy and Performance Estimation Strategy [17].

Search Space: This consists of the possible neural architectures the algorithm will search through. In our study, we consider shallow networks only. For the initial runs we considered two convolutional layers and one fully connected layer with the hyperparameters as the number of kernels and filter size for each layer and the number of dense connected units. Later, we increased this and the algorithm had to decide between 2 to 5 hidden layers and the number of kernels and filter size in each.

Search Strategy: This deals with the algorithm to navigate the search space. The most popular strategies are Random, Bayesian Optimization [18] and HyperBand Tuner[19].For our study, we decided to use Bayesian Optimization since it would be too computationally expensive to do an exhaustive search or a RandomSearch.

Performance Estimation Strategy: A normal Train-Test validation was investigated since we have a small dataset.

## RESULTS AND DISCUSSION

All the hyperparameters were first tested with a standard 1D CNN containing 2 hidden layers and 2 fully connected layers to get a good estimate of hyperparameters to do the neural architecture search.

### Hyperparameters

#### Batch size

The best batchsize tends to depend a lot on the learning rate and strongly on the optimization algorithm used but a general trend was the the error increased as the batch size increased. For the majority of test cases a batchsize of 8 or 16 gave the best results.

#### *Epochs*

The best epoch size was found manually from the loss graphs.Most of the models were found to converge in between 200 to 300 epochs so an epoch count of 300 was chosen.

#### *Learning rate*

For learning rate we implemented a function which reduced learning rate during training if the loss plateaued for a certain number of epochs. Two learning rates of 0.01 and 0.001 were tested and the learning rate would become half if the loss was stagnant for 10 epochs or more. For all test cases a lower learning rate of 0.001 gave better results and the learning rate plateau function was triggered frequently.

#### *Optimization algorithms*

All the optimization algorithms were run twice for different sets of the above hyperparameters. SGD appeared to be very

unstable and did not converge at all. All the optimization algorithms had much better performance at a lower learning rate of 0.001 than 0.01 except Adagrad which seemed to be an exception on repeated testing. All the algorithms performed best at batchsize = 8 except Nadam which gave pretty even performance for both 8 and 16.

Adam, Adamax and Nadam had the best values of RMSE at learning rate equal to 0.001 with Nadam being the most consistent through its runs. RMSProp gave comparable RMSE values but was very unstable and gave very different values of error for each run. Finally due to its stability across different runs and low RMSE values we decided upon Nadam as the preferred optimization algorithm with a learning rate of 0.001 and a batchsize of 8 or 16.

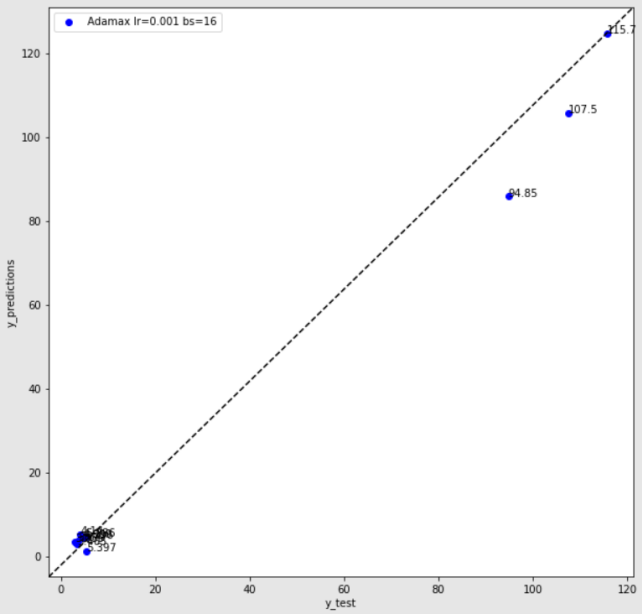


**Figure 1.** predicted viscosity vs actual viscosity for standard neural network with Adamax,learning rate=0.001,batchsize=16

**Table 3:** Results of initial hyperparameter optimization. [RMSE values on right; where lr: learning rate, bs: batch size.]

| Optimization Algorithm | $lr=10^{-2}$ bs=8 | $lr=10^{-2}$ bs=16 | $lr=10^{-3}$ bs=8 | $lr=10^{-3}$ bs=16 |
|---|---|---|---|---|
| Adadelta | 70 | 83 | NA | NA |
| RMSProp | 201.68 | 207.89 | 33.67 | 22.474 |
| Adagrad | 80.964 | 75.736 | 333.67 | 132.11 |
| Adam | 2349.1 | 2349.1 | 30.408 | 30.527 |
| Adamax | 105.75 | 2827.6 | 114.96 | 5.59 |
| Nadam | 150.72 | 252.11 | 5 | 22 |

## Neural Architecture Search

Since very low RMSE values of around 5 to 20 was achieved during our initial hyperparameter process with just two layers, there were concerns of overfit if the number of layers were increased and hence the search space was limited to 2 hidden layers and one dense layer. The search space is as follows.

**Table 4**: Architecture of 1D CNN used for hyperparameter testing.

| Hyperparameter | Search Space |
|---|---|
| layer1_filters | [32,64,96,128...256] step=32 |
| layer1_kernels | [2,4,8,16,24,32] |
| layer2_filters | [32,64,96,128...256] step=32 |
| layer2_kernels | [2,4,8,16,24,32] |
| Dense Layer | [32,48,64,80,96,112,128] |

An exhaustive search of all the possible combinations of the architecture would be too computationally expensive so Bayesian Optimization for the search was used.

The best results are as follows:

**Table 5:** Results of hyperparameter optimization of the neural network using Bayesian Neural Architecture Search

| layer1_filters | layer1_kernels | layer2_filters | layer2_kernels | Dense | RMSE |
|---|---|---|---|---|---|
| 32 | 16 | 256 | 8 | 128 | 6.12 |
| 32 | 16 | 224 | 2 | 128 | 9.45 |
| 32 | 12 | 256 | 4 | 128 | 16.5 |
| 32 | 32 | 256 | 2 | 96 | 7.2 |
| 32 | 32 | 256 | 2 | 64 | 8.5 |
| 32 | 32 | 256 | 2 | 80 | 13.6 |
| 32 | 32 | 256 | 2 | 48 | 28.6 |

Multiple runs of Bayesian Optimization was run and the best values for filters of layer 1 and 2 were 32 and 256. From the results we can see layer 1 preferred to be the minimum value of 32 consistently while for layer 2 the number of filters was always in the higher range above 200. The results are in Table 5.

For Kernels we see more variation but the trends suggest that layer 1 kernels prefer to be at the maximum end around 16 and layer 2 kernels prefer to be in the lower range mostly 2,4 and 8.

A run of Bayesian Optimization was done to confirm this where the layer1 and layer2 filters were fixed at 32 and 256. The results showed that layer 1 preferred to be a higher value of 32 and layer 2 stayed around 2 or 4. These results are in Table 6.

A run of Bayesian Optimization was done without Gaussian Noise and it gave much worse average performance than previous runs and the trend of hyperparameters were inconsistent thus showing that Gaussian Noise is important.

**Table 6:** Results of optimization of the number of kernels using Bayesian Neural Architecture Search

| l1_kernel | l2_kernel | RMSE |
|---|---|---|
| 32 | 4 | 5.86 |
| 32 | 2 | 10.629 |
| 16 | 2 | 66.776 |
| 2 | 8 | 70.496 |

## ACKNOWLEDGEMENTS

The project is funded by Natural Sciences and Engineering Research Council under Alliance Grants number R3839A44.

## REFERENCES


1. Abdulkadir I, Uba S, Almustapha MN. A Rapid Method of Crude Oil Analysis Using FT-IR Spectroscopy. *Nig. J. Basic Appl. Sci.* 24(1):47-55 (2016).
2. Speight J, Handbook of Petroleum Product Analysis: Second Edition (2015).
3. Larter SR, Aplin AC. Reservoir geochemistry: methods, applications and opportunities. *Geol. Soc. Lond.* 86(1):5–32 (1995).
4. Sánchez-Brito M, Luna-Rosas FJ, Mendoza-González R, Mata-Miranda MM, Martínez-Romo JC, Vázquez-Zapién GJ. A machine-learning strategy to evaluate the use of FTIR spectra of saliva for a good control of type 2 diabetes. *Talanta* 221:121650 (2021).
5. Alizadeh S, Ta S, Ray AK, Lakshminarayanan S. Determination of Density and Viscosity of Crude Oil Samples from FTIR Data using Multivariate Regression, Variable Selection and Classification. *IFAC-PapersOnLine* 55(7):845–850 (2022).
6. Ng W, Minasny B, Montazerolghaem M, Padarian J, Ferguson R, Bailey S, McBratney AB. Convolutional neural network for simultaneous prediction of several soil properties using visible/near-infrared, mid-infrared, and their combined spectra. *Geoderma* 352:251–267 (2019).
7. Kawamura K, Nishigaki T, Andriamananjara A, Rakotonindrina H, Tsujimoto Y, Moritsuka N, Rabenarivo M, Razafimbelo T. Using a one-dimensional convolutional neural network on visible and near-infrared spectroscopy to improve soil phosphorus prediction in Madagascar. *Remote Sens* 13(8):1519 (2021).
8. Prilianti KR, Setiyono E, Kelana OH, Brotosudarmo THP. Deep chemometrics for nondestructive photosynthetic pigments prediction using leaf reflectance spectra. *Inf. Process. Agric.* 8(1):194–204 (2021).
9. Bjerrum EJ, Glahder M, Skov T. Data Augmentation of Spectral Data for Convolutional Neural Network (CNN) Based Deep Chemometrics. *arXiv preprint* arXiv:1710.01927 (2017).
10. O'Shea K, Nash R. An Introduction to Convolutional Neural Networks. *arXiv preprint* arXiv:1511.08458 (2015).
11. Albawi S, Mohammed TA, Al-Zawi S. Understanding of a convolutional neural network. in *Proceedings of 2017 International Conference on Engineering and Technology (ICET) 1-6 (2017)*.
12. Bjerrum EJ, Glahder M, Skov T. Data Augmentation of Spectral Data for Convolutional Neural Network (CNN) Based Deep Chemometrics. *arXiv preprint* arXiv:1710.01927 (2017).
13. Srivastava N, Hinton G, Krizhevsky A, Salakhutdinov R. Dropout: A Simple Way to Prevent Neural Networks from Overfitting. *J. Mach. Learn. Res.* 15(1):1929-1958 (2014).
14. Kiranyaz S, Avci O, Abdeljaber O, Ince T, Gabbouj M, Inman DJ. D Convolutional Neural Networks and Applications-A Survey. *Mech. Syst. Signal Process.* 151:107398 (2021).
15. Ruder S. An overview of gradient descent optimization algorithms. *arXiv preprint* arXiv:1609.04747 (2016).
16. Abadi M, Agarwal A, Barham P, Brevdo E, Chen Z, Citro C, Corrado GS, Davis A, Dean J, Devin M, Ghemawat S. TensorFlow: Large-Scale Machine Learning on Heterogeneous Distributed Systems. *arXiv preprint* arXiv:1603.04467 (2016).
17. Elsken T, Metzen JH, Hutter F. Neural Architecture Search: A Survey. *J. Mach. Learn. Res.* 20(1):1997-2017 (2019).
18. Kandasamy K, Neiswanger W, Schneider J, Poczos B, Xing E. Neural Architecture Search with Bayesian Optimisation and Optimal Transport. *Adv. Neural Inf. Process. Syst.* 31 (2018).
19. Li L, Jamieson K, Rostamizadeh A, Talwalkar A. Hyperband: A Novel Bandit-Based Approach to Hyperparameter Optimization. *J. Mach. Learn. Res.* 18(1):6765-6816 (2017).


This conference proceeding has not been peer reviewed.



CSChE Systems & Control Transactions

Open Access | Original Research

**Conference Proceedings**
Canadian Chemical Engineering Conference 2022
October 23-26, Vancouver, BC, Canada

PSEcommunity.org/LAPSE:2022.0090

PSE PRESS

# High-Resolution Non-Contact Microwave Sensor for Water-Cut Measurements

**Bushra Kamal[a,b], Zahra Abbasi[b*], Hassan Hassanzadeh[a*]**

[a]Department of Chemical & Petroleum Engineering, Schulich School of Engineering, University of Calgary, Calgary, Alberta T2N 1N4, Canada
[b]Department of Electrical and Software Engineering, Schulich School of Engineering, University of Calgary, Calgary, Alberta T2N 1N4, Canada
* Corresponding authors: zahra.abbasi@ucalgary.ca, hhassanz@ucalgary.ca

## ABSTRACT

A novel, real-time, non-contact, non-invasive and high-sensitivity planar microwave sensor is developed for water cut measurements of crude oil samples. This sensor demonstrates the capability of measuring water cut of bitumen in real-time, which is of low-cost and eliminates the hurdles of current measurement techniques, prevents loss of production, and paves the way for oil field automation. The platform of the proposed sensor is based on a passive split ring resonator-based sensor with a defected ground gap coupled transmission line as the reader. The performance of the microwave sensor has been verified with varying water concentration in oil samples. The non-contact nature and high-resolution of the proposed structure enables monitoring of water cut in the full range.

**Keywords:** water cut measurement, planar microwave sensor, non-contact sensing, production monitoring

**Date Record:** Original manuscript received October 15, 2022. Published October 19, 2022.

## INTRODUCTION

The oil-water two-phase flow is commonly found in the petroleum exploration, production and development of oil fields. Monitoring the composition of the fluid, especially the water cut is vital [1]. Precise measurement of water content can improve the production surveillance [1] and optimize production processes [2]. The accurate measurement can aid in the quality control of the oilfields production operations, monitor the condition of oil wells, minimize energy consumption, and automate the oil fields [3]. The classical offline methods such as distillation, Karl-Fischer titration and centrifuge require the samples to be taken offline to laboratories for analysis which lengthens the measurement cycle and can potentially delay crucial operational recommendations to be made regarding certain processes in the petroleum industry [4]. With the advancement in technology, online water cut meters have gradually been developed over decades which are commonly based on capacitance measurement, gamma ray attenuation, density difference or infrared spectroscopy [2]. Amongst these methods, microwave technology has gained the attention of various researchers in academia as well as in the industry. This technique is robust and precise with full-range water cut measurement despite drift in the instrument [2].

Recently, planar microwave sensors have gained considerable attention as potential candidates because of the several compelling advantages that they offer, such as a simple and unique fabrication process, easy integration into the circuit, [5] low-cost, high-quality factor, [6] non-contact and real-time sensing capability [5]. These sensors are versatile and have been employed in a wide variety of applications ranging from oil and gas industries, optical sensing, pH sensing, gas concentration monitoring and chemical detection to volatile organic compound sensing [5-7].

Here, we propose a fast and reliable approach using planar microwave sensors to measure the water cut of the oil-water emulsions due to the numerous advantages that they offer. The principle of operation in the microwave sensor is based on the variation in the dielectric properties of the sample under the test, which is impacted by the water content in the mixture. A coupled reader-tag pair sensing approach is proposed, which enables sensing and monitoring in harsh environments. The tag is the main sensing element and can tolerate high temperatures and this property is immensely useful in harsh environments. The design of the ground engineered gap coupled transmission line as the reader is such that it can be placed at an arbitrary distance from the tag sensor and monitor the variation of water content in the sample around the tag while protecting the sensor from high temperature environment. The tag is chipless, battery-less, passive split-ring resonator sensor, which was fabricated on a flexible substrate of 0.254 mm thickness. The tag can be mounted on a container while the reader is fabricated on a more rigid substrate of thickness 1.575 mm purchased from Rogers Corporation.

## EXPERIMENTAL SECTION

Two emulsion samples, including water/pentane and water/bitumen were used for water cut measurements. Pentane employed in the experiment was purchased from VWR

Chemicals Ltd with a purity of ≥ 99%. For the water/bitumen case, 170 g of Mackay River bitumen was mixed with 30g of toluene (17 wt.%) to allow the formation of workable oil/water emulsion at room temperature. The toluene is used as the carrier phase for bitumen, and its volume was subtracted from the oil phase in water cut measurements. The setup consisted of the sensor, a mixer for homogenizing the solvent mixture at a constant RPM, a beaker containing the mixture of oil & water and a Vector Network Analyzer (VNA), which records the data and shows the variation of the sample that is changing around the tag.

The core principle of operation of this sensor can be explained using equation (1).

$$f_r \approx \frac{c}{2l\sqrt{\varepsilon_{eff}}} \quad (1)$$

where $c$ is the speed of light (m/s), $l$ is the tag's length and $\varepsilon_{eff}$ is the overall effective permittivity of the tag sensor. According to the above equation, increasing the effective permittivity of the material under test decreases the resonance frequency of the tag relatively. The variation in the effective permittivity will cause the resonance frequency to shift upward/downwards depending on the sample under test. As the mixture inside the tube changes from pure water ($\varepsilon_{eff}$ = 80) to samples with more oil (Bitumen/Pentane: $\varepsilon_{eff}$ = 2.6/1.84) concentration, the effective permittivity around the tag thereby increases.

In this experiment, three concentrations of pentane/water emulsion samples were prepared and examined by varying the concentration of pentane in water, and four different samples were prepared for the bitumen-water mixture. The beaker containing the mixture was stirred under the mixer for an average of two minutes to create a perfectly homogenized mixture. The tag was mounted on the container, and the sensor's frequency response for the mixture was observed and recorded in the VNA. Increasing the concentration of the different samples affects the effective permittivity of the mixture during the test. This change in permittivity is brought about by the tag, which senses the variation of the material around it and wirelessly communicates it to the reader in the circuit. The reader receives the signals, and the VNA then records the shift in frequency response of the sensor. The concentration of pentane was determined up to 90% in water which clearly establishes the robustness of this planar sensor, and the concentration of water was varied up to 28.57% in the bitumen sample by gradually adding 20 g of water in each step.

Figure 1 depicts the variation in the resonance profile of pentane/water emulsion under test in v/v%. Figure 2 shows the variation of water concentration in the bitumen sample in w/w%. Based on the reference material and the increasing concentration of pentane sample, the effective permittivity reduces, and we observe an upshift in the frequency response as expected. Based on equation (1), for the bitumen-water emulsion, the addition of more water increases the overall effective permittivity, and we observed a downshift in the resonance frequency.

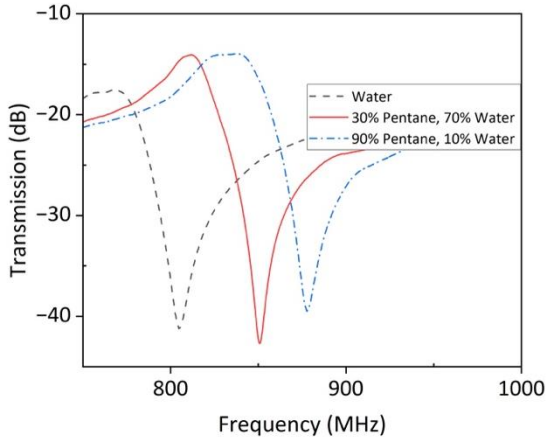


**Figure 1.** Resonant frequency profile for 3 different effective permittivities of Pentane-water mixture.

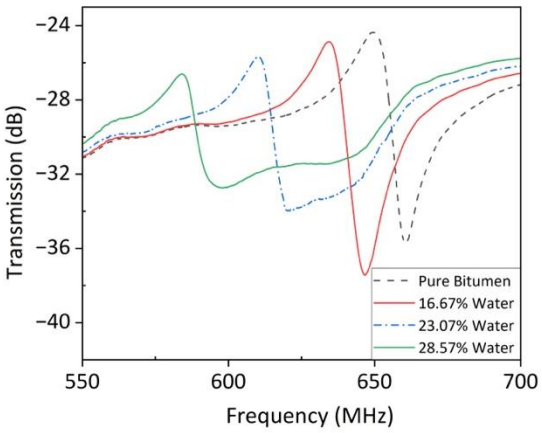


**Figure 2.** Transmission response of the sensor to varying concentration of water in bitumen sample.

The proposed sensor is a promising candidate for real-time monitoring, and label-free sensing of hydrocarbons for water cut measurement in the petroleum industry. The versatility of this sensor clearly demonstrates its potential for detecting other hydrocarbons for solvent detection and water cut measurements.

## CONCLUSION

This work presents a novel technique for detecting solvents and water concentration in the petroleum industry using a non-contact high-resolution microwave sensor measuring in real-time. The experimental results confirm the potential of this sensor for its high sensitivity and quality-factor for detection by varying concentration of hydrocarbons in water. The resonance frequency was the main variable considered for studying the sensor's response to changes in the concentration of the hydrocarbons. This technique produced promising results and is a low-cost microwave sensor with a sensing capability that could be extended for the detection of other hydrocarbons in water as well.

## ACKNOWLEDGMENT

The authors acknowledge the financial support of the Natural Sciences and Engineering Research Council of Canada and all member companies of the SHARP Research Consortium: Canadian Natural Resources Limited (CNRL), Cenovus Energy, ConocoPhillips, CNOOC International, Husky Energy, Imperial Oil Limited, Kuwait Oil Company, Osum Oil Sands, Strathcona Resources, and Suncor Energy. In addition, the support of the Department of Chemical and Petroleum Engineering and the Department of Electrical and Software Engineering at the University of Calgary is highly appreciated.

## REFERENCES

1. Yang Y, Xu Y, Yuan C, Wang J, Wu H, Zhang T. Water cut measurement of oil–water two-phase flow in the resonant cavity sensor based on analytical field solution method. *Measurement* 174:109078 (2021).
2. Sharma P, Lao L, Falcone G. A microwave cavity resonator sensor for water-in-oil measurements. *Sens. Actuators B: Chem.* 262:200-210 (2018).
3. Guowang G, Dasen H, Hua L, Wang F, Li Y. Research Status and Development Trend of Water Cut Detection Methods for Crude Oil. *J. Phys.: Conf. Ser.* 1894(1):012093 (2021).
4. Liu Q, Chu B, Peng J, Tang S. A visual measurement of water content of crude oil based on image grayscale accumulated value difference. *Sensors* 19(13):2963 (2019).
5. Abbasi Z, Baghelani M, Daneshmand M. Glycerol Concentration Monitoring Using High-resolution Non-contact RF Sensor. *IEEE Sensors*:1-4 (2020).
6. Baghelani M, Abbasi Z, Daneshmand M, Light PE. Non-invasive Lactate Monitoring System Using Wearable Chipless Microwave Sensors with Enhanced Sensitivity and Zero Power Consumption. *IEEE Trans. Biomed. Eng.* (2022).
7. Abbasi Z, Baghelani M, Daneshmand M. High-resolution chipless tag RF sensor. *IEEE Trans. Microw. Theory Tech.* 68(11):4855-4864 (2020).

This conference proceeding has not been peer reviewed.



CSChE Systems & Control Transactions

Open Access | Original Research

**Conference Proceedings**
Canadian Chemical Engineering Conference 2022
October 23-26, Vancouver, BC, Canada

PSEcommunity.org/LAPSE:2022.0091

PSE PRESS

# Prediction of Amines Thermal Degradation in $CO_2$ Capture Process Using Intelligent Techniques

**Abbas Azarpour[a]* and Sohrab Zendehboudi[a]**

[a] Memorial University, Department of Process Engineering, St. John's, NL, Canada
* Corresponding Author: azarpour@mun.ca.

## ABSTRACT

Mitigation of carbon emissions is an important step to achieve the climate change goals. Amine-based post-combustion $CO_2$ capture (PCC) process is a promising technology, and many commercial projects have been developed based on different capture mechanisms governing in various carbon capture and storage (CCS) processes. The thermally regenerative amine-based PCC is a traditional technology, which consists of an absorber to capture $CO_2$ from the flue gas and a desorber to strip $CO_2$ from the $CO_2$-rich. Although there have been substantial improvements in the industrial applications of amines technology, further developments are still required owing to significant energy requirement, high capital cost, and amine degradation. One of the most critical issues in the amine-based PCC process is the degradation of solvent, which occurs by the transformation of amines into other chemical components by thermal degradation and oxidative degradation. In the thermal degradation, the amines react with $CO_2$ to form compounds having high molecular weight, and in the oxidative degradation, the amines react with $O_2$ to synthesize compounds having low molecular weight. In addition, the high stable salts are formed as a result of the reaction between the amines and the carboxylic acids. These high stable salts lead to considerable problems in the regeneration process, and increase the chance of corrosion in the process equipment. Monoethanolamine (MEA) is the most recognized solvent, which is considered a benchmark solvent in the solvent-based PCC processes. It has been confirmed that to absorb one molecule of $CO_2$ two molecules of MEA are required, producing ion pair of $MEACOO^-$ (carbamate) and $MEAH^+$ (protonated MEA). In this research, the MEA thermal degradation is investigated through employing hybrid intelligent techniques of artificial neural network-particle swarm optimization (ANN-PSO) and coupled simulated annealing-least square support vector machine (CSA-LSSVM). The models development is carried out utilizing experimental data, and the input parameters are MEA concentration, $CO_2$ loading, temperature, and time, and the output is the remaining MEA concentration after experiencing the degradation phenomenon. The results can be employed for the further improvement of a solvent-based PCC process in terms of energy efficiency and operation cost. More importantly, the findings of this study can be used for the detailed and more accurate modeling and optimization of the corresponding processes.

**Keywords**: Amines, $CO_2$ capture, intelligent model, thermal degradation, statistical analysis

**Date Record:** Original manuscript received October 16, 2022. Published October 19, 2022.

## INTRODUCTION

Carbon capture and storage (CCS) is an unavoidable strategy to decelerate the climate change progress and meet the expectations of Paris Agreement [1-4]. Although there have been substantial developments in the industrial applications of amine technology, additional enhancements are still needed due to their high energy requirement, significant capital cost, and amine degradation [5, 6]. One of the most concerning issues in the amine-based PCC processes is the degradation of solvent, which occurs by the transformation of amines into other chemical components due to the chemical reactions. This adverse phenomenon takes place by the thermal degradation and oxidative degradation. In thermal degradation, the amines react with carbon dioxide to synthesize compounds having high molecular weight, and in oxidative degradation, the amines react with $O_2$ to form compounds having low molecular weight. In addition, high-stable salts are formed because of the reaction between the amines and the carboxylic acids. These high-stable salts create greater problems on the regeneration process and enhance the chance of corrosion in the process equipment [7]. Monoethanolamine (MEA) is the most common solvent, which is considered as a benchmark solvent, in the solvent-based PCC processes. In the capture process, MEA is wasted via thermal degradation, oxidative degradation, and volatility losses. Thermal degradation occurs by the polymerization of carbamate, causing high molecular weight by-products. Oxidative degradation, which takes place

in the stripper leading to the high-stable salts, is not a usual concern in the current applications of the amines absorption/stripping as oxygen is not in the system. The solvent losses due to the volatility in the absorber and stripper can be prevented through using a sophisticated control system [8]. In the $CO_2$ capture process, thermal degradation mostly occurs in the stripper, and significant research works have reported that high temperature in the presence of $CO_2$ is the key reason of degradation. Some studies stated that the thermal degradation occurs due to the high temperature in the absence of $CO_2$, emphasizing the essential role of heat. This type of degradation leads to dimerization, cyclization, and dealkylation. The main products of the thermal degradation of MEA are oxazolidine-2-one (OZD), N-(2-hydroxyethyl)imidazolidine-2-one (HEIA), N-(2-hydroxyethyl) ethylenediamine (HEEDA), and N,N'-bis-(2-hydroxyethyl)urea. Oxidative degradation normally occurs in the absorber, and the major reactions taking place are addition, piperazinones, and dealkylation. Some of the key products of the MEA oxidative degradation are ammonia, formaldehyde, acetaldehyde, methylamine, formamide, formic acid, glyoxal, and acetic acid [9]. There have been several research investigations on the solvents' degradation employed in the carbon capture processes. For instance, Davis and Rochelle [10] quantified the MEA thermal degradation as a function of $CO_2$ loading, temperature, and initial MEA concentration over the normal operating condition of the stripper. They concluded that most of the MEA loss happens in the formation of N,N'-bis-(2-hydroxyethyl)urea, HEEDA, and HEIA [10]. Thermal degradation and $CO_2$ removal capacity of various samples of MEA were evaluated at 160 °C over the period of 2-8 weeks. It was found that the concentration of MEA decreases by 95% because of the thermal degradation at 160 °C for 8 weeks ; however, the remaining solvent keeps its capacity at 22% to remove $CO_2$ [11]. Development of a $CO_2$ capture process model was carried out incorporating the degradation rate of MEA resulted from the experimental data. The model was used to assess the effect of the operating conditions on the process solvent loss. It was claimed that the major reason of solvent loss was the oxidative degradation in the absorber, while thermal degradation was not an important concern [12].

In another study, the researchers concluded that the developed method could be employed for the simultaneous quantification of various products of thermal degradation [13]. Molecular mechanisms demonstrating the thermal degradation of MEA were examined by employing molecular dynamic simulation as well as metadynamics sampling. It was found that the OZD formation as an intermediate and the main products of HEEDA and HEIA are thermodynamically favorable [14]. The literature review reveals that no investigation based on smart techniques has been carried out on the solvent thermal degradation analysis in a solvent-based PCC process. Thus, this research focuses on this gap employing the hybrid intelligent models. The models can offer an appropriate platform for the assessment of the solvent degradation in the proposed system, and the models can be utilized for the modeling and optimization of the solvent-based PCC processes.

# METHODOLOGY

## Data Processing

Adequate number of data is required for the accurate prediction of the solvent degradation. The key step of constructing a smart model is to determine the model input and output parameters. In this study, MEA initial concentration, time, $CO_2$ loading, and temperature are the input variables, and the MEA concentration left after particular period of time is the output variable. Thermal degradation greatly depends on the system temperature, and it happens at high temperatures. $CO_2$ loading increases the thermal degradation, and higher loading of $CO_2$ appears to enhance the thermal degradation either by improving the proton donors availability by catalyzing the dehydration or through the formation of more carbamate [15]. Concerning the effect of time, the products of thermal degradation usually increase over time [16]. Clearly, the solvent concentration in the system is a key parameter in the solvent thermal degradation. For example, an increase in the MEA concentration unexpectedly lowers the thermal degradation rate [8].

## Programming

MATLAB software is employed to build the models of artificial neural network-particle swarm optimization (ANN-PSO) and coupled simulated annealing-least square support vector machine (CSA-LSSVM). Various configurations of each model are used to obtain the reliable results. In the proposed models, the degradation of MEA is analyzed utilizing the input data and inputs. All data are normalized within the range of [-1 1] in order to prevent the numerical overflow in the program runs and achieve the required convergence. The following equation is used to normalize the data:

$$\hat{x} = 2\frac{x_i - x_{min}}{x_{max} - x_{min}} - 1 \quad (1)$$

where $\hat{x}$ refers to the normalized value of $x_i$, and $x_{min}$ and $x_{max}$ resemble the minimum and maximum values of the experimental data.

## Model Performance Assessment

The statistical parameters including mean square error (MSE), average absolute relative error percentage (AARE%), and coefficient of determination ($R^2$) are used to assess the precision and performance of the models. The following equations introduce the above-stated statistical measures [17-19]:

$$AARE\% = 100 \sum_{i=1}^{n} \left| \frac{x_d^i - x_m^i}{x_d^i} \right| / n \quad (2)$$

$$MSE = \frac{1}{n} \sum_{i=1}^{n} \left( x_d^i - x_m^i \right)^2 \quad (3)$$

$$R^2 = 1 - \frac{\sum_{i=1}^{n} \left( x_d^i - x_m^i \right)^2}{\sum_{i=1}^{n} \left( x_d^i - \bar{x} \right)^2} \quad (4)$$

where $x_d^i$ and $x_m^i$ are the amounts of the experimental data and predicted by the model; $\bar{x}$ stands fot the average value of the experimental data; and $n$ indicates the data number.

# RESULTS AND DISCUSSION

Various parameters are optimized to configure the most optimal ANN-PSO model, such as constants for *gBest* and

*pBest*, number of particles, number of maximum iterations, and number of neurons in the hidden layer. Figure 1 displays the performance of the ANN-PSO model for the data sets of training and testing. The values of AARE% for the training and testing phases are 6.57 and 5.33, respectively. The LSSVM model with the radial Kernel function contains two critical parameters of tuning ($\sigma^2$) and regularization ($\gamma$), and their optimal values are computed by CSA optimization algorithm. These two parameters substantially affect the model prediction accuracy. The estimated optimal values of $\sigma^2$ and $\gamma$ are 218.52 and $2.89\times10^5$, respectively. Figure 2 illustrates the performance of the CSA-LSSVM model in the training and testing phases. The AARE% values for the data sets of training and testing are 3.30 and 5.36, respectively.

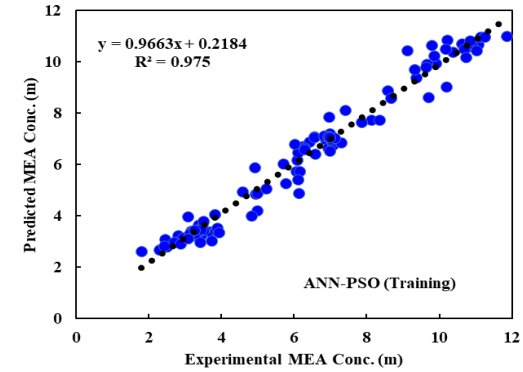


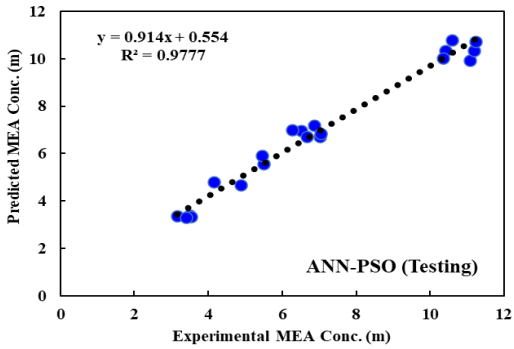


**Figure 1.** Performance of ANN-PSO.

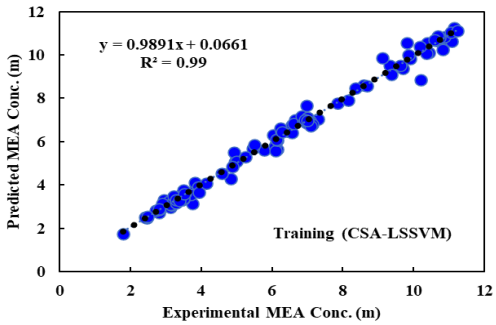


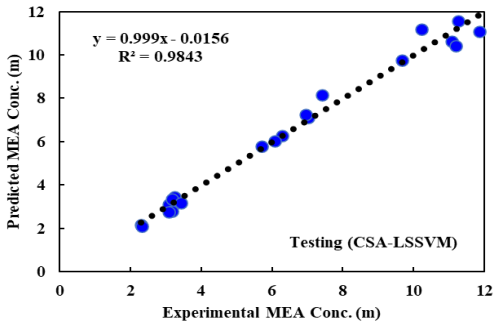


**Figure 2.** Performance of CSA-LSSVM.

## Comparison of Developed Models

The statistical criteria of $R^2$ (coefficient of determination), AARE%, and MSE are employed to assess the developed models performance. Figure 3 depicts the performance of ANN-PSO and CSA-LSSVM based on training and testing data sets. Table 1 reports the developed models performance based on the statistical criteria, revealing that CSA-LSSVM is a more accurate model.

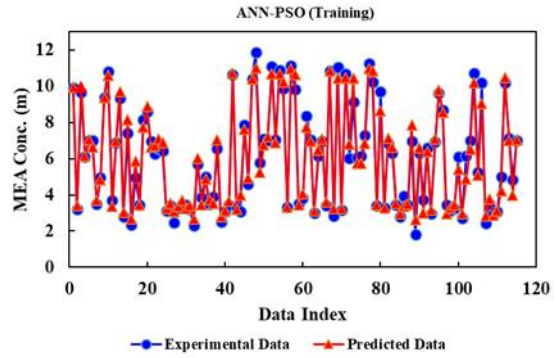


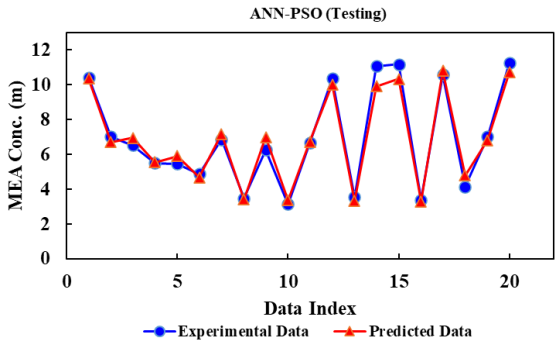

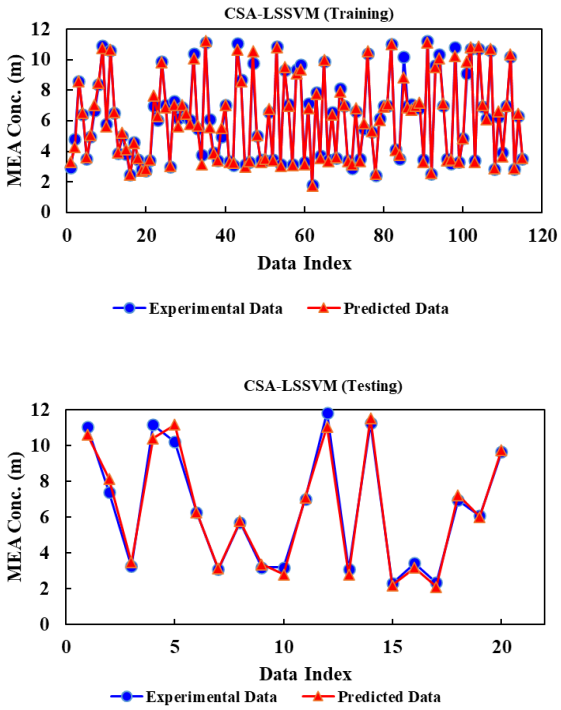


**Figure 3.** Performance of the models based on the training and testing phases.

**Table 1:** Performance of the developed models.

| Model | $R^2$ (Tr) | $R^2$ (Ts) | MSE (Tr) | MSE (Ts) | AARE % (Tr) | AARE % (Ts) |
|---|---|---|---|---|---|---|
| ANN-PSO | 0.975 | 0.977 | 0.195 | 0.211 | 6.57 | 5.33 |
| CSA-LSSVM | 0.990 | 0.984 | 0.073 | 0.176 | 3.30 | 5.36 |

## Parametric Sensitivity Analysis

Sensitivity analysis is performed to figure out the relationship between the input variables and the output variable. Correlation matrix theory can determine the degree of the linear relationship between two variables in a multi-variable system. Different approaches can be utilized to compute the strength of the linear relationship. The Pearson product-moment correlation coefficient is one of the most suitable techniques to do the correlation matrix analysis. The analysis reveals that the variables of temperature, loading, and time have a negative relationship with the output variable, indicating that an increase in these variables decreases the remaining concentration of the solvent in the system. Temperature has the strongest negative relationship with the target variable.

In the solvent-based PCC operation, it was claimed that 10% of the operation cost is associated with the solvent degradation [20]. This suggests the significance of understanding amine degradation in the performance analysis of the PCC processes. Moreover, the capacity of solvent to absorb $CO_2$ reduces when it faces the unfavorable phenomenon of degradation. The byproducts of the degradation should be removed from the system. They are hazardous wastes, and their quantity and specifications require to be determined for the more accurate control of the process. Moreover, a suitable model of the thermal degradation outside of the customary operating conditions is needed to optimize the system [21]. Increasing temperature accelerates the MEA degradation, and in a constant pressure system, lower $CO_2$ concentration leads to the elevated temperature of the reboiler, leading to the thermal degradation enhancement [8]. An increase in MEA concentration increases the risk of corrosion, and results in increased viscosity of the solution. Based on the results obtained by Davis [8], an increase in temperature results in more thermal degradation while increasing $CO_2$ loading and amine concentration reduces the thermal degradation. In this research, increase in temperature and $CO_2$ loading accelerates the thermal degradation while an increase in MEA concentration lowers the thermal degradation. Thus, there is a discrepancy between the two models with respect to the $CO_2$ loading. However, the results of this study regarding the influence of $CO_2$ loading on the thermal degradation agree with the models developed by Braakhuis, Høisæter [15] and Léonard, Toye [22].

## CONCLUSIONS

In this research, amines thermal degradation in the conventional solvent-based post-combustion $CO_2$ capture (PCC) process was analyzed by employing the hybrid intelligent models of ANN-PSO and CSA-LSSVM. Moreover, a correlation was introduced using the capability of the GEP based on the concept of maximum fitness and optimal evolution. The training phase reveals that CSA-LSSVM model is more accurate than ANN-PSO. The results indicate that increase in temperature, $CO_2$ loading, and time accelerate the thermal degradation, and an increase in initial the MEA concentration results in the reduction of the thermal degradation. Considering the global warming, together with the several solvents capable of absorbing $CO_2$ and extreme cost of experimental activities, this research offers a convenient groundwork for a systematic analysis of the thermal degradation mechanism of the solvents and more precise development of the optimization models. The developed methodology together with the developed models can be employed for the prediction of thermal and oxidative degradation of various solvents and the comparison of their capability in $CO_2$ absorption. The selected suitable solvent can be used to optimize the standard PCC processes employing the first principle models and/or intelligent techniques.

## REFERENCES

1. Neveux T, Le Moullec Y, Corriou JP, Favre E. Modeling CO2 capture in amine solvents: Prediction of performance and insights on limiting phenomena. *Ind. Eng. Chem. Res.* 52(11):4266-4279 (2013).
2. Oh HT, Lee JC, Lee CH. Performance and sensitivity analysis of packed-column absorption process using multi-amine solvents for post-combustion CO2 capture. *Fuel* 314:122768 (2022).
3. Zhang W, Ma C, Li H, Xuan L, An A. Dmc-pid cascade control for mea-based post-combustion CO2 capture process. Chem. Eng. Res. Des. 182:701-713 (2022).
4. Zendehboudi S, Khan A, Carlisle S, Leonenko Y. Ex situ dissolution of CO2: A new engineering methodology based on mass-transfer perspective for enhancement of CO2 sequestration. *Energ. Fuel.* 25(7):3323-3333 (2011).

5. Wang C, Jiang K, Jones TW, Yang S, Yu H, Feron P, Li K. Electrowinning-coupled CO2 capture with energy-efficient absorbent regeneration: Towards practical application. *J. Chem. Eng.* 427:131981 (2022).
6. Dashti A, Raji M, Razmi A, Rezaei N, Zendehboudi S, Asghari M. Efficient hybrid modeling of CO2 absorption in aqueous solution of piperazine: Applications to energy and environment. *Chem. Eng. Res. Des.* 144:405-417 (2019).
7. Maeda N, Kishimoto A, Machida H, Yamaguchi T, Yanase K, Norinaga K. Durability and fire-hazardous-risk evaluation of unique phase separation solvent using high-boiling-point amine and ether. *Int. J. Greenh. Gas Control.* 114:103532 (2022).
8. Davis JD. Thermal degradation of aqueous amines used for carbon dioxide capture. The University of Texas at Austin: USA (2009).
9. Gouedard C, Picq D, Launay F, Carrette FL. Amine degradation in CO2 capture. I. A review. *Int. J. Greenh. Gas Control.* 10:244-270 (2012).
10. Davis J, Rochelle G. Thermal degradation of monoethanolamine at stripper conditions. *Energy Procedia* 1(1):327-333 (2009).
11. Zoannou KS, Sapsford DJ, Griffiths AJ. Thermal degradation of monoethanolamine and its effect on CO2 capture capacity. *Int. J. Greenh. Gas Control.* 17:423-430 (2013).
12. Léonard G, Crosset C, Toye D, Heyen G. Influence of process operating conditions on solvent thermal and oxidative degradation in post-combustion CO2 capture. *Comput. Chem. Eng.* 83:121-130 (2015).
13. Cuccia L, Bourdon R, Dugay J, Bontemps D, Carrette PL, Vial J. Novel approach for the quantitative analysis of mea degradation products present in gas effluent of CO2 capture process by thermal desorption–gas chromatography–mass spectrometry: Development and validation. *Int. J. Greenh. Gas Control*. 60:110-119 (2017).
14. Yoon B, Stowe HM, Hwang GS. Molecular mechanisms for thermal degradation of CO2-loaded aqueous monoethanolamine solution: A first-principles study. *Phys. Chem. Chem. Phys.* 21(39):22132-22139 (2019).
15. Braakhuis L, Høisæter KK, Knuutila HK. Modeling the formation of degradation compounds during thermal degradation of mea. *Ind. Eng. Chem. Res.* 61(7):2867-2881 (2022).
16. Andrzej W, Spietz T, Wieklaw-Solny L, Krotki A, Tarnowska J. Degradation of amine solvents used for CO2 removal from flue gas with high CO2 concentration. *Architecture, Civil Engineering, Environment* 14(1):115-124 (2021).
17. Balasubramanian K, Ananthamoorthy NP. Improved adaptive neuro-fuzzy inference system based on modified glowworm swarm and differential evolution optimization algorithm for medical diagnosis. *Neural. Comput. Appl.* 33(13):7649-7660 (2021).
18. Zare M, Zendehboudi S, Abdi MA. Deterministic tools to estimate induction time for methane hydrate formation in the presence of luvicap 55 w solutions. *J. Mol. Liq.* 348:118374 (2022).
19. Pham H. A new criterion for model selection. *Mathematics* 7(12):1215 (2019).
20. Rao AB, Rubin ES. A technical, economic, and environmental assessment of amine-based CO2 capture technology for power plant greenhouse gas control. *Environ. sci. technol.* 36(20):4467-4475 (2002).
21. Oyenekan BA, Rochelle GT. Energy performance of stripper configurations for CO2 capture by aqueous amines. *Ind. Eng. Chem. Res.* 45(8):2457-2464 (2006).
22. Léonard G, Toye D, Heyen G. Experimental study and kinetic model of monoethanolamine oxidative and thermal degradation for post-combustion CO2 capture. *Int. J. Greenh. Gas Control*. 30:171-178 (2014).

This conference proceeding has not been peer reviewed.



CSChE Systems & Control Transactions

Open Access | Original Research

**Conference Proceedings**
Canadian Chemical Engineering Conference 2022
October 23-26, Vancouver, BC, Canada

PSEcommunity.org/LAPSE:2022.0092

PSE PRESS

# Prediction of Different Crude Oil Properties from FTIR Data with Statistical Methods, Deep and Shallow Neural Networks

**Shahla Alizadeh[a*], Souvik Ta[a], Ajay. K. Ray[a] and Lakshminarayanan Samavedham[b]**

[a] Western University, Department of Chemical and Biochemical Engineering, London, Ontario, Canada
[b] National University of Singapore, Department of Chemical and Biomolecular Engineering, Singapore, Singapore
* Corresponding Author: salizad7@uwo.ca.

## ABSTRACT

In recent years, Fourier Transform InfraRed (FTIR) spectrometry has been widely used to estimate different characteristics and contents of materials in many fields. Even though numerous works have been published in this area, it has still been difficult to suggest a global method that can predict the properties of crude oils from different resources based solely on FTIR data. In this study, we compare the application of several methods in order to predict particular important properties (i.e., viscosity, density, total sulfur content, total acid number, etc.) of crude oil samples from seven different Canadian oil fields. We employed chemometric methods such as Partial Least Squares regression (PLS) and principal component regression (PCR) and compared the results to the performance of neural networks (NN) with a different number of layers. These methods were evaluated by calculating the coefficient of determination ($R^2$) and prediction root mean squared errors (RMSE). Although less complicated statistical methods like PCR and PLS could lead to excellent predictions for some properties, we found that neural networks could improve the results in other properties. In addition, the prediction accuracy of some properties, like viscosity, was improved by classification before the application of regression methods.

**Keywords**: FTIR, Crude Oil Properties, Statistical Methods, Deep Neural Network, Shallow Neural Network, Chemometric Methods

**Date Record:** Original manuscript received October 15, 2022. Published October 19, 2022

## INTRODUCTION

An accurate determination of specifications of crude oil as the essential source of the world's fossil fuel is vital in the oil industry. Since petroleum is a complex mixture of organic compounds, its quality is mostly evaluated by physicochemical properties [1]. These properties are of high interest for addressing many reservoir engineering and operational process problems.

American Society for Testing and Materials (ASTM) and American Petroleum Institute (API) have standard methods for reporting crude oil analysis. So, these properties are ideally determined experimentally on actual fluid samples via elaborate laboratory procedures, which are mostly expensive and not too eco-friendly.

Accordingly, it is of high value to propose methods for both reliable and rapid evaluation of crude oils, which can estimate properties without any sample preparation so more eco-friendly, and with less labor work. In this work, we propose the best chemometric methods and neural networks using FTIR spectroscopy for simultaneously reliable and rapid determination of crude oil properties.

Owing to rapid and significant advances in multivariate statistics and machine learning techniques, it is now possible to estimate many properties of interest (that are difficult or costly to measure) using other relatively simpler, faster, and less expensive measurements. Analytical procedures which are less dependent on sample size [2] are now available for mapping out the relationship between the easily available measurements, such as Fourier Transform InfraRed (FTIR), and the difficult to obtain measurements, such as the viscosity of crude oil.

## METHODS

Stepping towards incorporating FTIR data into physicochemical properties, we studied the data of one hundred and seven crude oil samples obtained from seven different Canadian oil fields that a petroleum company in Canada supplied. They obtained the FTIR spectra corresponding to these samples using a Thermo Fisher FTIR microscope. They also measured several physicochemical properties of these crude oil samples using appropriate analytical instruments. The company wants to develop robust models that can only provide accurate estimates of the physicochemical properties utilizing FTIR data, thus avoiding the need for elaborate, expensive, and time-consuming laboratory procedures.

We analyzed the application of several methods to predict particular important properties of crude oil samples by randomly dividing data into training, calibration, and test sets. We employed chemometric methods such as Partial Least Squares regression (PLS) and principal component regression (PCR) and compared the results to the performance of neural networks (NN) with a different number of layers. We evaluated these methods by calculating the coefficient of determination ($R^2$) and prediction root mean squared errors (RMSE).

These results have been partially reported in a separate study involving eighty-two crude oil samples focused on predicting viscosity and density with chemometric methods [1].

## DISCUSSION

This study focuses on the importance of spectra data in predicting the physicochemical properties of crude oil samples from different oil fields. We suggest the best methods, including chemometric ones, like PLS and PCR, and varying depth neural network ones, to calculate several important crude oil properties, like viscosity, density, total acid number, total sulfur content, etc., disrespect of analyzing a light oil or a heavy one.

## ACKNOWLEDGEMENTS

The authors gratefully acknowledge the financial support from Natural Sciences and Engineering Research Council of Canada (NSERC).

## REFERENCES

1. Alizadeh S, Ta S, Ray AK, Lakshminarayanan S. Determination of Density and Viscosity of Crude Oil Samples from FTIR Data using Multivariate Regression, Variable Selection and Classification. *IFAC PapersOnLine* 55(7):845-850 (2022).
2. Rocha JT, Oliveira LM, Dias JC, Pinto UB, Marques MDLS, Oliveira BP, Filgueiras PR, Castro EV, de Oliveira MA. Sulfur determination in Brazilian petroleum fractions by mid-infrared and near-infrared spectroscopy and partial least squares associated with variable selection methods. *Energy & Fuels* 30(1):698-705 (2016).

This conference proceeding has not been peer reviewed.



CSChE Systems & Control Transactions

Open Access | Original Research

**Conference Proceedings**
Canadian Chemical Engineering Conference 2022
October 23-26, Vancouver, BC, Canada

PSEcommunity.org/LAPSE:2022.0093

PSE PRESS

# Inflation- and Energy-Adjusted Historical Prices Reflect Disruptive Events to Global Energy Systems

**Thomas A. Adams II**[a*]

[a] Norwegian University of Science and Technology, Department of Energy and Process Engineering, Trondheim, Norway
* Corresponding Author: thomas.a.adams@ntnu.no

## ABSTRACT

The historical prices of oil, coal, and natural gas in the United States after adjusting for energy content and inflation are computed and provided in a comparative context from 1984 to the present (August 2022). The price history reflects impacts by disruptive local or global events. Although current oil and gas prices are high, when adjusted for inflation, they are still not as high as prices experienced during the early 1980s and late 2000s. However, high global inflation rates compound other factors that are increasing energy prices now, leading to record high prices in absolute terms, and sticker shock to consumers worldwide. The recent impacts of the pandemic, Texas Freeze, and Russian invasion of mainland Ukraine are evident. Although oil and gas generally trend up or down together, they remain decoupled on an energy basis as they have been since 2006.

**Keywords**: oil price, gas price, coal price, inflation, energy

**Date Record:** Original manuscript received October 12, 2022. Published October 21, 2022.

## INTRODUCTION

Everyday consumers are usually most directly connected to global energy systems through fuel and energy purchases, particularly electricity, heating, and transportation fuels. The actual prices paid by consumers can have major impacts on public policy, economic activity, and simply daily life. Memories are short, and it is easy to believe that things are the worst they have ever been (especially just before US midterm elections). Therefore, it is useful to look at price history to understand if the changes we have been experiencing are common or unique.

Prices reflect reality, and therefore they are useful measurements that give hints as to what is going on with the larger global energy system. By looking at prices on an inflation-adjusted and energy-adjusted basis, one can understand how changes in technology and disruptive world events impact our relationship with energy and the interactions between its different forms. One can also ascertain the relative health of our energy system from this information, and perhaps heed the warnings it might provide. Therefore, I present inflation-adjusted and energy-adjusted historical prices since 1984 are with an analysis in the context of world events and the resiliency of the larger global energy system.

## METHODOLOGY

### Natural Gas

Data for natural gas uses the average US Natural Gas Price at the city gate expressed in USD per thousand cubic feet published by the US Energy Information Administration in various Monthly Energy Review reports, using the most recent data set available [1]. Residential customers have typically paid about 100% to 300% more than the city gate price in the past three years, which includes delivery charges to the home and other factors. The variability in residential prices compared to city gate prices is presently the highest it has been in the past 40 years. Although wellhead prices are no longer tracked in the dataset, the city gate price historically was typically anywhere between 20 to 200% higher than the price of gas at the wellhead.

The city gate price is chosen as the representative price because it avoids the additional complications associated with contracts, transportation, and delivery to the customer, as noted by its lower volatility compared to the other two metrics. After removing the data points related to the February 2021 Texas Freeze incident, the average absolute value of the percent change in price from month to month of all data available since 1976 is only 5.7% per month for the city gate, compared to 6.3% for the wellhead and 6.8% for the residential customer after delivery. Similarly, the interquartile range (the difference between the third quartile and first quartile) of absolute percentage monthly price change for the city gate is the lowest as well at 6.0%, compared to 7.7% for the residential price.

The price per standard cubic feet was converted to price per GJ by assuming an average energy content of 1037 BTU per cubic foot of natural gas on a higher heating value (HHV) basis. The energy content can vary from this depending on the specific blend of gases that comprise it from day to day. The

value chosen was approximately the average value in the US from 2015-2021 with very little variation, noting that it is slightly higher (1%) than the previous twelve years [2] due to small changes in composition.

### Coal

The coal price data was sourced from the US Energy Information Administration, which was listed in USD per short ton (1 short ton = 2000 lbs ≈ 907.18 kg) for four different types of coal, including both thermal and metallurgical coals [4, 5]. Quarterly data for steam coal exports was available from 2016 and annual data for domestic coal prior to it. The price used for "coal" in this study is a weighted "basket" of steam coal prices (a.k.a. thermal coal, used for energy purposes) consisting of 75 wt% bituminous coal, 8% lignite, and 17% anthracite coals. The heating values of bituminous, lignite, and anthracite coals were assumed to be 35, 17, and 35 $GJ_{HHV}$/tonne (1 tonne = 1000 kg) respectively (which uses a medium-rank bituminous heating value) [6-8]. Note that heating values will vary wildly from coal to coal but variations in the numbers do not alter the interpretation of the resulting plots much.

### Oil

Oil prices used in this analysis are the composite prices for the refiner's acquisition cost of crude, provided on a monthly basis in USD per barrel [1]. The composite prices reflect both domestic and imported crudes. This is appropriate because it reflects the price of the oil purchased either domestically ("first purchase price") or internationally ("free on board cost") plus transportation and other costs associated with getting the oil to the refinery. The refinery acquisition composite cost is the most appropriate for comparison to the natural gas city gate and thermal coal export prices in this context. There is no distinction in oil quality (composition, API gravity, sweetness, etc.), and so an average heating value of 6.12 $GJ_{HHV}$ per barrel of oil equivalent is used to determine the price on an energy content basis.

### Inflation

Inflation adjustments were made using the appropriate consumer price index (CPI) value for that month [3]. For reference, January 1914 had an index of 10 and the years 1982 to 1984 collectively have a CPI of 100 by definition. All US Dollar prices were adjusted to August 2022, which has an index of 296.171. The overall CPI metric is used, not energy, specifically so that the changes in energy prices compared to the rest of the economy can be easily seen. For example, the CPI for August 2022 was 8.4%, but the CPI for the Energy Commodities is a whopping 27.1% [3].

## RESULTS

The resulting inflation adjusted US energy prices are shown in Figure 1, on a $USD_{August2022}$ per $GJ_{HHV}$ basis.

### Gas and Oil Remain Decoupled

**Table 1:** Selected inflation and energy adjusted oil and gas price relationships. R is the correlation between oil and gas prices. O–G is the average relative price premium of oil over gas. Trend Match is the percentage of months when oil and gas both moved in the same direction (+/-) compared to the previous month.

| Period | R | O–G | Trend Match |
|---|---|---|---|
| 1984-2005 | 0.786 | 17% | 49% |
| 1992-2005 | 0.828 | 14% | 32% |
| 2008-Aug 2022 | 0.583 | 152% | 58% |

As discussed in a 2015 work [9], oil and gas prices were fully coupled from 1984 (and in fact much before it) until 2006, when hurricane Katrina significantly disrupted oil networks and its price. Essentially, prior to 2006, visual inspection shows that oil and gas were very similar in price per energy content at any time. Exceptions are seen in a few places, such as from impacts on oil (and not gas) of the Persian Gulf War in August 1990, but the correlation from 1984 to 2005

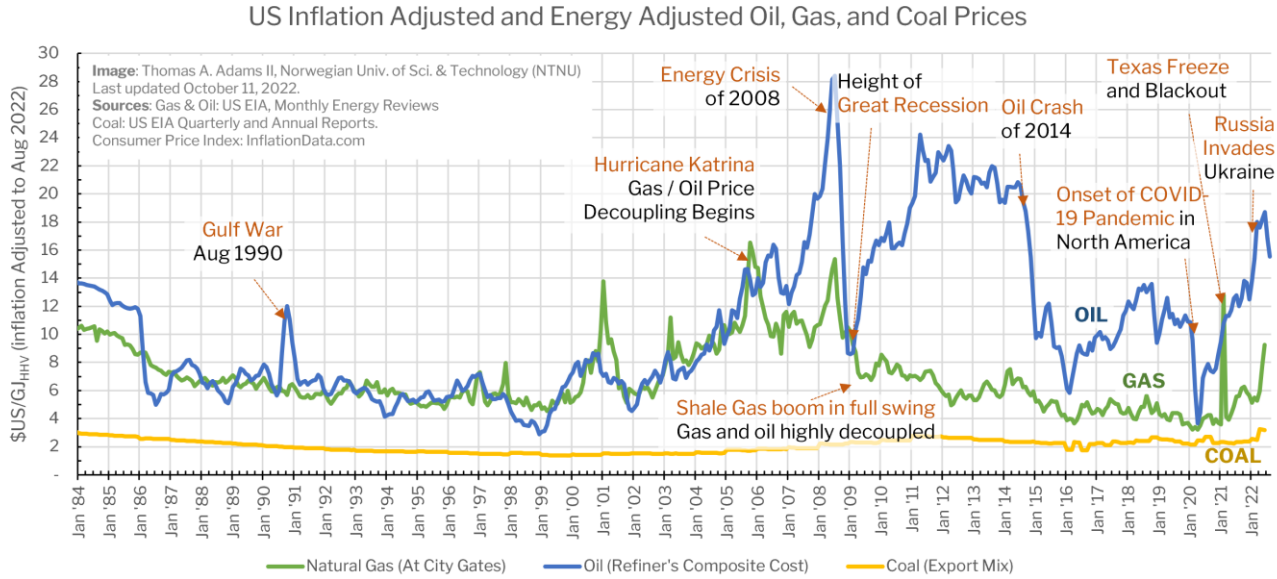


**Figure 1.** Comparative inflation adjusted prices of natural gas, oil, and coal in the United States. Selected disruptive events are noted. See text for methdology.

(inclusive) is a remarkable $R = 0.786$, as shown in Table 1. It was particularly highly correlated after the Persian Gulf War impacts resided (1992 to 2005 inclusive). However, after the shale gas boom takes full swing in 2008, the correlation drops precipitously—only $R = 0.583$ from 2008 to the present.

The relative price of oil to gas ("O-G") shown in Table 1 is computed as follows:

$$"O - G" = \frac{P_{oil} - P_{gas}}{P_{gas}} \quad (1)$$

where $P_{oil}$ and $P_{gas}$ are the inflation and energy adjusted prices of oil and gas in $USD_{Aug2002}$ per $GJ_{HHV}$. Prior to 2005, the oil price on an energy adjusted basis was on average roughly 17% higher than the price of gas (using the particular prices chosen), but after 2008 the oil been on average 152% higher per $GJ_{HHV}$ than gas. Thus, the decoupling has been consistent and persistent since the shale gas boom, signaling a permanent change in global energy systems.

The "Trend Match" statistic shows the percentage of months in which oil and gas both trended in the same direction as compared to the previous month. This is interesting because when taken into comparison with $R$, short term and long term trends can be separated. For the highly correlated period after the Gulf War but before the shale boom (1992-2005), the trend match is low at only 32%. This can be interpreted that this period shows that generally speaking the oil and gas prices were strongly correlated at the macro or long term level, but at the micro level, they were not. Essentially, there is some market noise and other factors here which only has small impacts when comparing the two fuels. In fact, the price direction changes are likely anti-correlated, since the trend match should be 50% for completely random walks.

Contrast this with the post-shale boom period (2008-present), which has the least correlated prices, but the highest trend match at 58%. This means that although certain events might drastically change one price (but not the other) at the macro level (and then sustain it), oil and gas prices are much more correlated in the short term. In other words, they now tend more to rise and fall together in the short term, indicating that and noise or technical difference impacts on price are somewhat overcome by other day-to-day factors that impact energy more generally.

## Coal's Historically Stability and Relative Cost Unchanged

Coal remains remarkably stable compared to the other two fuels, even when considering that the data are only available on annual or quarterly amounts and so short term noise cannot be seen. Coal continues to be consistently lower in cost than oil or gas on an energy and inflation adjusted basis and relatively impervious to major world events until very recently.

It is no surprise then that $CO_2$ emissions from coal power reached an all time global high in 2021 [10] due in large part to its availability, low price, and stability. This record high $CO_2$ emissions from coal is even despite efforts in North America and Europe to drastically reduce coal use, improve efficiency, and even capture $CO_2$ emissions in some cases. Canada for example has reduced coal power generation from 2000 to 2021 by 66%, and Europe likewise by 41% [11]. These cuts have been more than offset by growth primarily in China and India, together which are responsible for almost two thirds of the world's coal power generation. They have increased coal power production by 404% and 226% over the same period [11].

## Impacts from the Pandemic

Three recent world events stand out strongly in the plot. The first is the impact of the pandemic on oil prices in North America. Billions of people across the world were either encouraged or forced to work from home or avoid travel, drastically reducing the demand for transportation fuels. The immediate plunge in oil price is evident, and it took all of 2020 to rebound to pre-pandemic levels. Headlines were made when West Texas Intermediate Futures contracts dropped below *negative* 40 USD per barrel on April 20, 2020 [12]. The demand became so low that there was insufficient storage available for upstream oil being produced, and companies had to pay to have it taken off their hands.

Gas prices in the pandemic actually increased somewhat over its February 2020 level, partly because it is not a major transportation fuel, and perhaps partly because it was needed for atypical peaking power generation uses due to drastic shifts in daily power demand cycles arising from massive changes in personal habits and behaviours.

## Impacts from the Texas Freeze

The Texas Freeze impacted gas prices severely in the United States, but did not affect the other two fuels significantly. In February 14-15, 2021, an extreme cold weather event occurred (extreme for Texas that is) in which parts of urban Texas were well below freezing for days at a time, the Dallas-Fort-Worth area reaching down to –2°F (–19°C). The energy infrastructure Texas is not built for that unusual amount of cold, and nearly 49% of Texas' electricity generation capacity was knocked out at the same time at its worst moments. Controlled outages were required, and some areas were more impacted than others because of difficulties in implementing rolling outages. By 1:20 AM on the 15th emergency operations reached their highest level.

The impact on the grid was massive. Electricity prices in Texas from Feb 14-19 2021 averaged at roughly $6600 USD per MWh (the price was typically about $21 per MWh the previous winter!) and returned to normal by the Feb 20 [13]. Despite the relatively brief outage in just one US State, the country's average gas price for the whole month went up 258%. It is the biggest single month impact on gas price in both absolute and relative terms for the entire data range.

## Impacts from Russia's Invasion of Ukraine

The 2022 invasion of Ukraine sparked more massive price fluctuations. Oil grew quickly over its already relatively high pre-invasion price, and gas had its third highest single month and two month percentage increases. Our Coal metric price reached an all time high (noting the annual and quarterly inflation adjusted prices used) in April 2022, shortly after the invasion. The coal price jump is significant because it reflects Europe's reliance on Russian oil and gas; prior to the invasion, the EU imported about 35% of its natural gas and about 25% of its oil from Russia [11].

Reductions in consumption of Russian imports (largely-self imposed by Europe for both punitive and other measures) caused increased demand for coal for power purposes. The subsequent impact on electricity prices is huge; electricity prices in Europe more than doubled since the invasion and are now about ten times as high as pre-pandemic prices.

## CONCLUSIONS

A review of energy price history using energy adjusted and inflation-adjusted metrics is instructive because it provides important insights into the health and interconnectedness of global energy systems. Although consumers may be faced with sticker-shock at the pump, the impacts of inflation are huge at present, and so in relative historical terms the oil price is not presently the "worst" it has ever been.

What is more telling is how recent disruptive world events seem to have more of an impact on our energy systems than in the past. The three major examples of the past two years each point to individual problems with the resiliency of our global energy infrastructure. The first resulted in the historical absurdity of massively negative oil futures prices, the second resulted in the single biggest price disruption in natural gas, and the third produced highest price of coal (all since 1984 and in inflation adjusted terms).

This is a canary in the coal mine. It should be a warning that our global energy systems are quite vulnerable to disruption and are already stretched with what is a regionally limited European war. Although the way the world responded to the pandemic was a unique event, a cold weather event in a single US state and a geographically restricted war are not unique in history. They are quite likely to happen again in even more serious fashion. We need better preparedness, or we will face far worse consequences in the near future.

The solutions need to be multi-faceted, and include improved foreign energy policy, energy security, energy supply chain robustness, energy independence, and the incorporation of alternative forms of energy for transportation and use. Diversification improves resiliency, and these approaches can all be done while pursuing greenhouse gas reduction goals. These are the most urgent challenges of the energy systems engineer.

## ACKNOWLEDGEMENTS

No funding was received for this work.

## REFERENCES

1. US Energy Information Administration. September 2022 Monthly Energy Review (2022).
2. US Energy Information Administration. July 2022 Natural Gas Monthly (2022).
3. US Bureau of Labor Statistics. Consumer Price Index. https://www.bls.gov/cpi/. Accessed October 2022.
4. US Energy Information Administration. Annual Coal Report, October 4 (2021)
5. US Energy Information Administration. Quarterly Coal Report, October 3 (2022)
6. Otto KC. Lignite. *Encyclopedia Britannica* (2016)
7. Otto KC. Anthracite. *Encyclopedia Britannica* (2020)
8. Otto KC. Bituminous Coal. *Encyclopedia Britannica* (2019)
9. Adams TA. Future opportunities and challenges in the design of new energy conversion systems. *Comput Chem Eng* 81:94-103 (2015).
10. International Energy Agency. Coal Fired Electricity (Sept 2022)
11. BP. Statistical Review of World Energy (2022).
12. Investing.com. Crude Oil WTI Futures Historical Data (Accessed October 2022).
13. ERCOT. Review of February 2021 Extreme Cold Weather Event – ERCOT Presentation (2021).



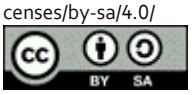

CSChE Systems & Control Transactions

Open Access | Original Research

**Conference Proceedings**
Canadian Chemical Engineering Conference 2022
October 23-26, Vancouver, BC, Canada

PSEcommunity.org/LAPSE:2022.0094

PSE PRESS

# Hemoglobin Response Modeling under Erythropoietin Treatment: Physiological Model-Informed Machine Learning Method

**Zhongyu Zhang[a] and Zukui Li[a]***

[a] University of Alberta, Department of Chemical and Materials Engineering, Edmonton, Alberta, Canada
*Corresponding Author: zukui@ualberta.ca

## ABSTRACT

Patients with renal anemia (RA) are usually treated with recombinant human erythropoietin (EPO) because of insufficient renal EPO secretion. The establishment of a good hemoglobin (Hgb) response model is a necessary condition for dose optimization design. The purpose of this paper is to apply physics-informed neural networks (PINN) to build the Hgb response model under EPO treatment. Neural network training is guided by physiological model to avoid overfitting problem. During the training process, the parameters of the physiological model can be estimated simultaneously. To handle differential equations with impulse inputs and time delays, we propose approximate analytical expressions for the pharmacokinetic (PK) model and weighted formulations for the pharmacology (PD) model, respectively. The improved PK/PD model was incorporated into PINN for training. Tests on simulated data show that the proposed method has good performance.

**Keywords**: Renal Anemia, Erythropoietin Therapy, Parameter Identification, Physics-Informed Neural Networks

**Date Record:** Original manuscript received October 15, 2022. Published October 21, 2022.

## INTRODUCTION

Renal anemia (RA) is a disease caused by the deficiency of erythropoietin (EPO) secretion by kidney. This is due to impaired renal function or some toxic substances in the plasma of uremic patients interfering with the production and metabolism of red blood cells [1]. It is a common complication of chronic kidney disease and a risk factor for cardiovascular complications. Now the efficacy of EPO in the treatment of RA has been well documented [2]. EPO is a glycoprotein with 165 amino acids. When oxygen delivery to specific cells within the kidney is reduced, secretion of EPO increases while circulating in the plasma and stimulating bone marrow progenitor cells, thereby increasing erythrocyte production [3]. If the increase in erythrocyte numbers relieves the hypoxic signal, EPO expression is downregulated. Despite its clinical effectiveness, there are potential drug-induced risks in patients treated with EPO. In practice, clinicians usually adjust the frequency and dose of EPO based on current hemoglobin (Hgb) measurements and previous dosing rules. It requires rich clinical experience. While low Hgb level leads to anemia, high Hgb levels can increase the risk of Hgb variation patterns and even mortality for the patient [4]. Therefore, it is important to develop decision support tools that can help the medical staff determine the appropriate dose and frequency of EPO to maintain the target Hgb level and reduce the cost of treatment.

To help physicians make patient-specific decisions on the optimal dosage of EPO treatment, a model that describes the Hgb response to the EPO dosing is necessary. Existing methods of erythropoiesis modeling can be divided into two main categories. One is physiologically driven modeling, which usually uses a combination of pharmacokinetic (PK) and pharmacodynamics (PD) models to describe the dynamics of Hgb concentration following the administration of intravenous EPO [5], [6], [7]. The other is data-driven modeling. It sets EPO dose data and Hgb measurements as input and output, respectively. Then data-driven models like neural network or autoregressive model can be trained to represent the erythropoiesis process [8], [9]. Both approaches have advantages and disadvantages. By building a physiologically driven model, we can get the details of the system states. Moreover, if the theoretical model is correct, the physiologically driven model can work well. But in practice, conventional method often has difficulties in estimating physiological parameters for ill-posed inverse problems [10]. On the other hand, although a data-driven model can approximate complex functions, it is sensitive to data noise and may not perform in prediction.

Given the above problems, this work aims to develop a more efficient method to build an erythropoiesis model. The proposed method uses physics-informed neural networks (PINN) to identify the physiological model parameters. Just like the framework of PINN proposed in paper [11], the front part of the neural network is similar to the ordinary fully connected neural network. With the network output and the associated gradients calculated from auto-differentiation, the physiological model equation residuals are incorporated in the loss function to enforce the physiological model information.

In this way, PINN achieves good estimation and robustness to noise and disturbances.

## PHYSIOLOGICAL MODEL

Regarding the Hgb response to EPO dosage, an example of clinical data record is shown in Figure 1. Hgb level is recorded around every 2 weeks, patients with late-stage renal disease receive EPO treatment 1 to 3 times per week [12].

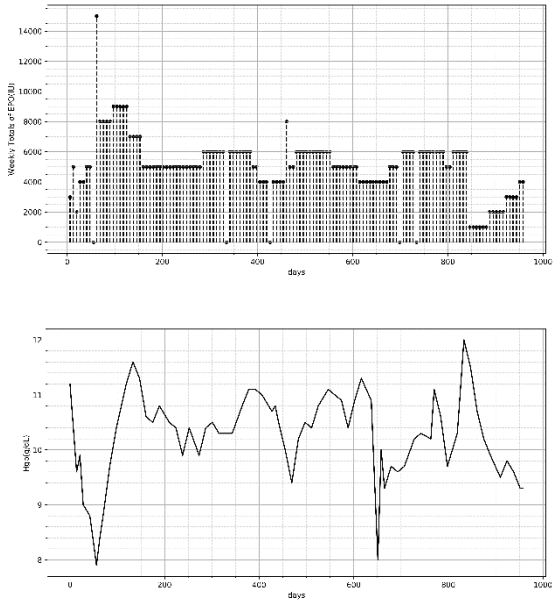


**Figure 1.** A clinical example data of EPO dosages and Hgb responses

Paper [13] has proposed a physiological erythropoiesis model to describe the Hgb-EPO relationship. The model consists of PK and PD model equations. The PK model describes how the body affects specific exogenous chemical substances through absorption and distribution mechanisms after drug administration, as well as changes in the metabolism of substances in the body, and the effects and excretion pathways of drug metabolites [14]. The PD model explains pharmacological effects on living systems, including reactions and binding to cellular components, and the biochemical and physiological consequences of these effects [15].

For the PK model, it can be described as:

$$\frac{dE(t)}{dt} = -\frac{V \cdot E(t)}{K_m + E(t)} - \alpha \cdot E(t) + dose(t) \quad (1)$$

$$E_p(t) = E(t) + E_{en} \quad (2)$$

$$k_{in}(t) = \frac{S \cdot E_p(t)}{C + E_p(t)} \quad (3)$$

$$\mathrm{E_{en}} = \frac{\mathrm{C \cdot H_{en}}}{\mu \cdot \mathrm{K_H \cdot S - H_{en}}} \quad (4)$$

The PD model is defined as bellow:

$$\frac{dR(t)}{dt} = k_{in}(t - D) - \frac{4x_1(t)}{\mu^2} \quad (5)$$

$$\frac{dx_1(t)}{dt} = x_2(t) \quad (6)$$

$$\frac{dx_2(t)}{dt} = k_{in}(t - D) - \frac{4x_1(t)}{\mu^2} - \frac{4x_2(t)}{\mu} \quad (7)$$

$$Hgb(t) = K_H \cdot R(t) \quad (8)$$

In the PK model equations, $E(t)$ denotes the amount of exogenous recombinant human EPO, $E_{en}$ denotes the endogenous EPO, $E_p(t)$ is the total EPO of the dynamic pool in plasma, $k_{in}(t)$ is the red blood cells (RBC) production rate, and $dose(t)$ is the EPO dosing in international unit (IU) which is modeled as a train of impulses.[13] Additionally, the model contains some parameters: $H_{en}$ is the Hgb level due to endogenous EPO, μ represents the mean RBC life span, $V$ is the maximum exogenous EPO clearance rate, $K_m$ stands for the exogenous EPO level that produces half-maximum clearance rate, α is the linear clearance constant, $S$ represents the maximal RBC production rate stimulated by EPO, $C$ is the amount of EPO that produces half-maximum RBC production rate [13].

In the PD model, states $R(t)$ represent the population of red blood cells (RBC), states $x_1(t)$ and $x_2(t)$ are internal states that aid in calculating $R(t)$, $Hgb(t)$ is the hemoglobin level which can be detected clinically, parameters $D$ is the time required for EPO-stimulated RBCs to start forming, $K_H$ is the average amount of Hgb per RBC (mean corpuscular hemoglobin, or MCH, in a complete blood count) which takes value of $K_H = 29.5pg/cell$ [13].

The initial conditions can be determined as below

$$R_0 = \frac{Hgb_0}{K_H} \quad (9)$$

$$x_{10} = \frac{\mu \cdot (H_{en} - \mu \cdot K_H \cdot \dot{R}_0)}{4K_H} \quad (10)$$

$$x_{20} = \frac{K_H \cdot R_0 - H_{en} + \mu \cdot K_H \cdot \dot{R}_0}{K_H} \quad (11)$$

Based on the above physiological model, eight unknown model parameters $\alpha, C, D, H_{en}, K_m, \mu, S, V$ can be estimated using collected data for each patient. In this work, we use the inverse PINN for the parameter estimation.

## PHYSICS-INFORMED MACHINE LEARNING

Paper [11] proposed the PINN which is a type of neural network trained to solve supervised learning tasks while following given physical law described by partial differential equations. It is shown by [16] that the method performs well to identify the unknown model parameters.

The PINN structure [17] used in this work is shown in Figure 2. Time is the input. States of the physiological system are output. The hidden layers perform nonlinear transformations on the data [18]. It is similar to a fully connected neural network but adds three extra layers to accelerate convergence. Input-scaling layer is designed to shrink the input time domain through a linear scaling function. When differential equations solution has a certain pattern, for example, the solution follows periodicity or attenuation, feature layer can be set as $sin(kt)$ or $e^{-kt}$ respectively [16]. If states have different magnitudes, the output-scaling layer can be used to scale them.

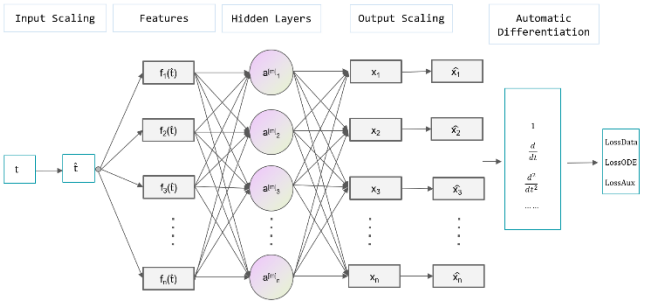


**Figure 2.** Physics informed neural networks architecture

The main idea of PINN is to incorporate the physical model equation residual (error) into the loss function of the neural network training. During the training process, the network model parameters and the physical model parameters can be estimated simultaneously. Consider a set of ODE equations

$$\frac{dx_s}{dt} = f_s(x_s, t; p) \qquad s = 1, \dots, S \tag{12}$$

The loss function is composed of 3 parts as follows.

$$Loss(\theta, p) = Loss^{data}(\theta) + Loss^{ode}(\theta) + Loss^{aux}(\theta) \tag{13}$$

where

$$Loss^{data}(\theta) = \sum_{m=1}^{M} w_m^{data} Loss_m^{data}$$

$$= \sum_{m=1}^{M} w_m^{data} \left[\frac{1}{N^{data}} \sum_{n=1}^{N^{data}} \left(y_m(t_n) - \widehat{x_m}(t_n;\theta)\right)^2\right] \tag{14}$$

$$Loss^{ode}(\theta) = \sum_{s=1}^{S} w_s^{ode} Loss_s^{ode}$$

$$= \sum_{s=1}^{S} w_s^{ode} \left[\frac{1}{N^{ode}} \sum_{n=1}^{N^{ode}} \left(\frac{d\widehat{x_s}}{dt}|_{\tau_n} - f_s(\widehat{x_s}(\tau_n;\theta), \tau_n; p)\right)^2\right] \tag{15}$$

$$Loss^{aux}(\theta) = \sum_{s=1}^{S} w_s^{aux} Loss_s^{aux}$$

$$= \sum_{s=1}^{S} w_s^{aux} [x_s(T_0) - \widehat{x_s}(T_0;\theta)]^2 \tag{16}$$

$N^{data}$ is the number of sample data points where both the input (time and additional control input) and the output response are available. $N^{ode}$ is the number of collocation points used to evaluate the model residual. Note that there is no response data needed for those collocation points. $Loss^{data}$ is difference values between measurements of $y_1, y_2, \dots, y_M$ and network outputs $\widehat{x_1}, \widehat{x_2}, \dots, \widehat{x_M}$ at time $t_1, t_2, \dots, t_{N^{data}}$. $Loss^{aux}$ is similar to $Loss^{data}$, but it specifically considers the start time point $T_0$ as an additional source. $Loss^{ode}$ is the key point of PINN. By automatic differentiation, the derivative of output states $\widehat{x_1}, \widehat{x_2}, \dots, \widehat{x_S}$ concerning input $t$ at the time point $\tau_1, \tau_2, \dots, \tau_{N^{ode}}$ can be obtained. Then we can calculate the residual error according to the differential equations and use it as a part of the loss function. In this way, differential equations are integrated into the neural network, which attaches physical constraints to machine learning. The weighting coefficients $(w_1^{data}, w_2^{data}, \dots, w_M^{data})$, $(w_1^{ode}, w_2^{ode}, \dots, w_S^{ode})$ and $(w_1^{aux}, w_2^{aux}, \dots, w_S^{aux})$ are used to balance the loss terms. Finally, by minimizing the loss function, the parameters θ of the neural network and unidentified parameters $p$ of differential equations are optimized together.

## MODIFIED PK/PD MODEL FOR PINN

To incorporate the physiological model into the PINN framework, we face two challenges from the original PK/PD model, which are explained below.

### Impulse input sequences in PK equations

Eq. 1 is a differential equation with impulse input sequence. This equation describes the decay process of exogenous EPO in the human body. Based on a simulation of this differential equation with parameter V, Km, α being set as 1660, 76.5, 0.25, respectively. Black dash-dot curve in Figure 3 illustrates the trajectory of EPO in human body during 10 days after receiving 7000 IU EPO medications on the second day. In practice, dose(t) is a train of impulses. This causes two issues when PINN is used to incorporate this physiological equation. First, the width of the impulse tends to be zero and the derivative $\frac{dE(t)}{dt}$ goes to infinity at the dosing time. It is impossible to directly evaluate the differential equation residual $\frac{dE(t)}{dt} - \left[-\frac{V \cdot E(t)}{K_m + E(t)} - \alpha \cdot E(t) + dose(t)\right]$. Secondly, the profile of $E(t)$ is not smooth under an impulse sequence input as shown in the figure. It is not very efficient to approximate this nonsmooth function through the neural network. To address this issue, we propose a method to approximate this differential equation based on the following observations.

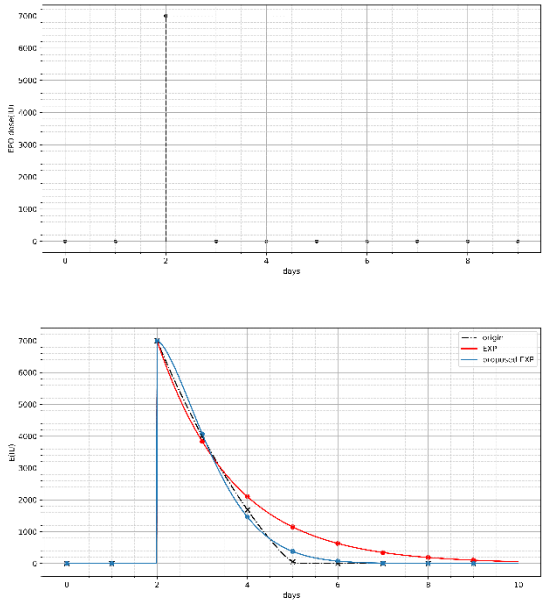


**Figure 3.** Trajectory of E(t) under a single EPO dosage

According to the differential equation 1, when $E(t)$ is much bigger than $K_m$, the equation can be simplified as

$$\frac{\mathrm{d}E(t)}{\mathrm{d}t} \approx -V - \alpha \cdot E(t) + dose(t) \tag{17}$$

For this equation, the solution trajectory of $E(t)$ is an exponential function as shown by the red line in Figure 3 with $\alpha = 0.6$. Compared with the exponential function, the curve of differential equation solution $E(t)$ decreases more quickly.

To improve the approximation accuracy, we propose the following exponential function Eq. 18 to approximate $E(t)$,

$$E(t) = \sum_{j=1}^{N(t)} dose_j \cdot exp\left[-\left(a_0 \cdot e^{\frac{-dose_j}{a_1}} + a_2\right) \cdot \left(t - t_j\right)^{a_3}\right] \tag{18}$$

where $a_0, a_1, a_2, a_3$ are four undetermined parameters, $t_j$ and $dose_j$ correspond to the $j$-th EPO administration time and dosage value, respectively. $N(t)$ is the total number of dosing times up to time $t$. For example, if the patient receives 5000 IU EPO treatment and 10000 IU EPO treatment on the 20th day and 60th day, the corresponding $(t_j, dose_j)$ are (20, 5000), (30, 10000). Using exponentiation of time difference, this proposed exponential function can match the differential equation solution better at the later stage.

To demonstrate the performance of the proposed model equation, we simulate the original equation 1 to get the profile of $E(t)$ under the EPO dose sequence as shown in the top part of Figure 3. Afterwards, we sample data from the true solution (as shown by the black dash-dot curve in Figure 3) and then use least squares method to estimate the parameters in the proposed model equation 18. The estimated parameter values are a0 = 1.87, a1 = 3640, a2 = 0.269, a3 = 1.53. The $E(t)$ trajectory calculated by the proposed exponential function Eq. 18 is drawn in Figure 3 by blue line, which approximates the true response curve (black dash-dot curve) very well.

In addition to the single impulse input study, the accuracy of the proposed model equation is also tested over a sequence of EPO dosages which was obtained from clinical data. The top part of Figure 4 is the EPO treatment record. The solution of the differential equation and the approximate exponential function are shown in the middle part of Figure 4, respectively. Notice that the bottom one is the zoomed version of the red box in the middle figure to show more details. $R^2$ of $E(t)$ prediction is equal to 99.76%. This result verifies that the proposed model equation approximates the original exponential differential equation very well.

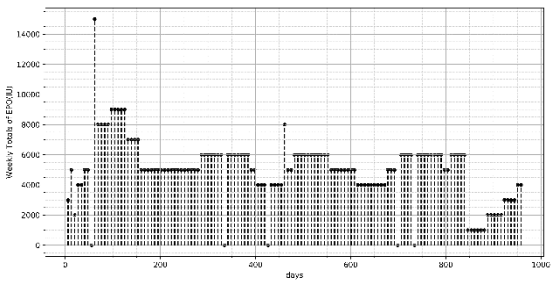


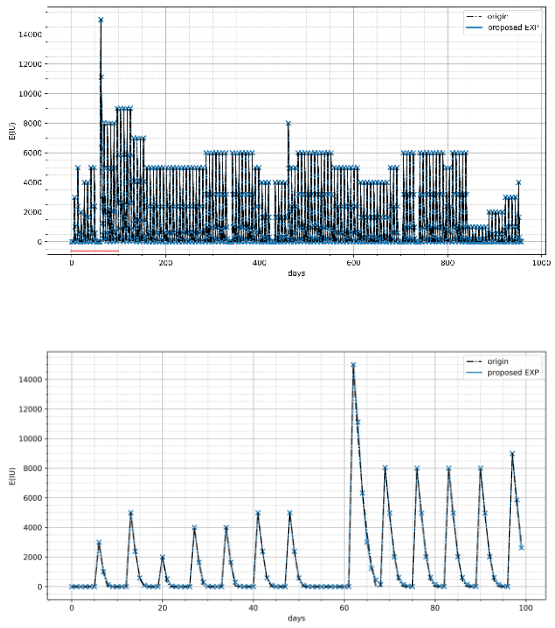


**Figure 4.** Trajectories of EPO in the body based on clinical data

## TIME DELAY IN PD EQUATIONS

The other issue comes from Eq. 5 and Eq. 7. These two equations are delay differential equations. The delay item $D$ is the parameter to be estimated. However, in the neural network, it is hard to calculate the partial derivative of the loss function with respect to the delay parameter.

Paper [13] has studied the low-pass filter nature of the RBC pool. As shown in Figure 5, a twice-weekly dosing sequence is simulated and it generates pulsatile and periodic EPO levels $E_P$ and corresponding production rate $k_{in}$; but the periodic dynamics are largely smoothed out by the low-pass nature of the RBC pool filter [13].

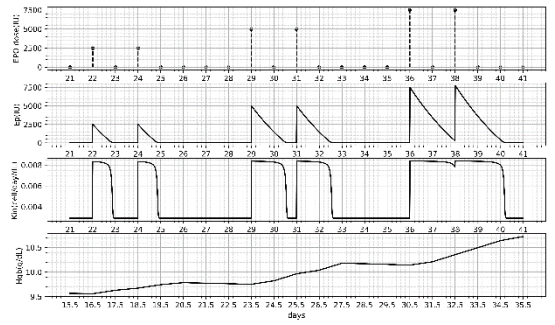


**Figure 5.** Low-pass nature of the RBC pool filter

Therefore, during the therapy, PK and cell production PD is relevant to the mean value of the production rate, which is denoted as $\overline{k_{\text{in}}}$ in Eq. 19 where $[iT, (i+1)T]$ is a single dose period. The Eq. 3 can be reconsidered as a memoryless nonlinear relationship between EPO doses and mean production rate

$\overline{k_{\text{in}}}$,[13] which means a similar mean production rate profile $\overline{k_{\text{in}}}$ will lead to similar Hgb trajectory.

$$\overline{k_{\text{in}}}(dose_i, T) = \frac{1}{T}\int_{iT}^{(i+1)T} k_{\text{in}}(t)dt \tag{19}$$

Based on the above analysis, we propose to convert the delay differential equations into a different form which makes the estimation easier. The method is based on a weighting function and the new equations are defined as follows:

$$\frac{dR(t)}{dt} = \lambda_1 k_{in}(t - D_1) + \lambda_2 k_{in}(t - D_2) - \frac{4x_1(t)}{\mu^2} \tag{20}$$

$$\frac{dx_2(t)}{dt} = \lambda_1 k_{in}(t - D_1) + \lambda_2 k_{in}(t - D_2) - \frac{4x_1(t)}{\mu^2} - \frac{4x_2(t)}{\mu} \tag{21}$$

$$\lambda_1 + \lambda_2 = 1 \tag{22}$$

The term $k_{in}(t - D)$ is replaced by the weighting function $\lambda_1 k_{in}(t - D_1) + \lambda_2 k_{in}(t - D_2)$, where $\lambda_1$ and $\lambda_2$ are parameters to be determined, and $D_1$ and $D_2$ are fixed as 4 and 7, respectively. This is based on the fact that the time required for progenitor cells to be stimulated by EPO and finally become reticulocytes ready to mature into RBCs is 4 - 7days [3]. The original delay parameter $D$ can be estimated as

$$D = \lambda_1 D_1 + \lambda_2 D_2 \tag{23}$$

Figure 6 shows the RBC production rate $k_{in}$ and the average weekly production rate $\overline{k_{\text{in}}}(T = 7)$ of the original form and the proposed weighting function respectively. Here, $\lambda_1$ and $\lambda_2$ are both set as 0.5. It illustrates that during every dose period, there is some difference between the original form $k_{in}(t - D)$ and the proposed weighting function $\lambda_1 k_{in}(t - D_1) + \lambda_2 k_{in}(t - D_2)$. For example, in the second dose period (day 22 to 29), the original model solution includes two pulses whereas the proposed weighting function produces three pulses with a smaller magnitude. However, the average weekly production rate $\overline{k_{\text{in}}}$ of the original form gets superimposed by the $\overline{k_{\text{in}}}$ of the proposed weighting function. The trajectories of Hgb level obtained from these two methods in this short term are similar, as shown in Figure 7.

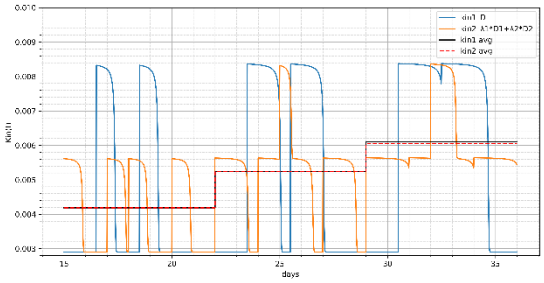


**Figure 6.** Comparison between the average weekly production rate $\overline{k_{\text{in}}}$ and $k_{in}$

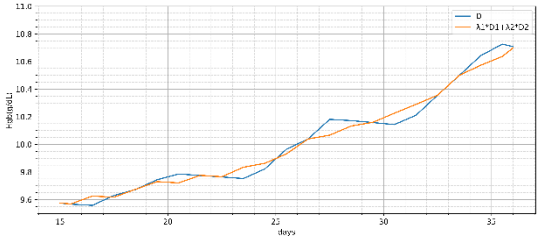


**Figure 7.** Hgb value of two methods in short term

**Table 1:** PARAMETERS FOR PK/PD MODELS

| $\alpha$ | $K_m$ | $V$ | $C$ | $D$ | $H_{en}$ | μ | $S$ |
|---|---|---|---|---|---|---|---|
| 0.25 | 46.5 | 2800 | 22.45 | 5.5 | 7.9 | 92.2 | 0.0084 |

Finally, we check the approximation performance over a long horizon. With parameters set as Table 1, the original model and the approximated model are both simulated. Figure 8 shows these two Hgb trajectories of the original form and delay differential equations with a weighting function. Root mean square error (RMSE) between two curves equals 0.0712.

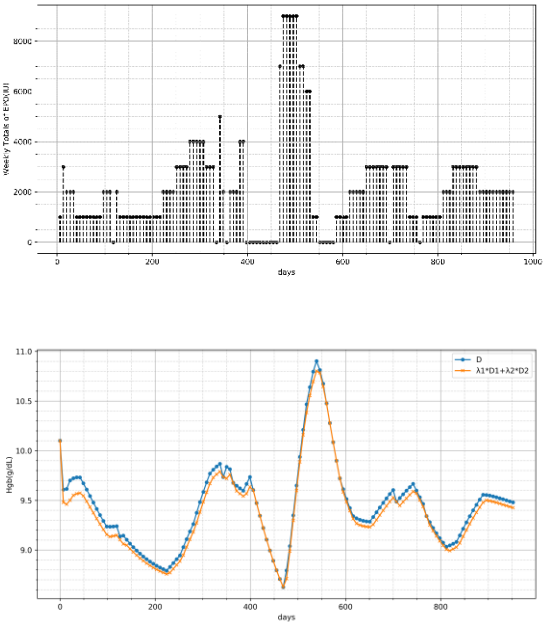


**Figure 8.** Long term Hgb responses: original model and approximation model

Above results show that the proposed PK/PD model modification approximate the original model very well. They provide a basis for the PINN modeling as described in the next section.

## PINN USING THE MODIFIED PK/PD MODEL

According to the proposed approximation model explained, the overall physiological model used in the PINN is based on equations 18, 2,3,4,20, 6, 21, 8.

**Table 2:** PINN1 (FROM NOISE-FREE DATA), PINN2 (FROM NOISY DATA

| | $\alpha$ | $K_m$ | $V$ | $C$ | $D$ | $H_{en}$ | $\mu$ | $S$ |
|---|---|---|---|---|---|---|---|---|
| True | 0.1 | 120 | 600 | 30 | 5.2 | 9 | 90 | 0.004 |
| PINN1 | 0.0959 | 127 | 607 | 27.6 | 5.36 | 8.89 | 95.0 | 0.00378 |
| PINN2 | 0.0966 | 127 | 616 | 30.2 | 5.38 | 9.07 | 84.6 | 0.00422 |

During the PINN training process, the neural network parameters and the parameters in the physiological model are simultaneously estimated. The loss term corresponding to the model residual is based on equation 20, 6, 21.

Based on the parameters $a_0, a_1, a_2, a_3$, original parameters $V, K_m, \alpha$ can be further estimated through least squares method. Besides, the delay parameter $D$ can be evaluated using equation 23.

## Test on simulated data

To demonstrate the proposed erythropoiesis modeling based on PINN, true parameter values as listed in Table 2 and a set of EPO input sequence as shown in Figure 9 are chosen to generate a series of Hgb data by solving this PK/PD model. Then Gaussian noise with zero mean and the standard deviation of $\sigma_\epsilon = c\mu$ is added to Hgb data to simulate measurement noise, where μ is the standard deviation of original Hgb data and c is equal to 5%. According to the noise-free Hgb data and the noise-containing Hgb data, we use PINN to identify these parameters in the differential equations separately and compare the results. The algorithm is implemented in Python with the open-source library DeepXDE [19]. The neural network is formed from 5 hidden layers and each one has 64, 128, 256, 128, 64 neurons. The feature layer adopts $t, sin(t), sin(2t), sin(3t), sin(4t), sin(5t)$. The swish function is set as the activation function. In addition, we use the Adam optimizer [20] and 500000 iterations with a learning rate equal to $10^{-4}$.

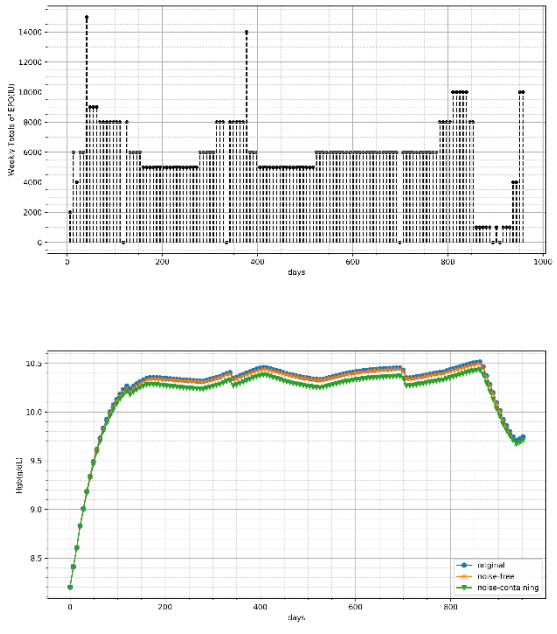


**Figure 9.** Simulated true Hgb responses and PINN model predictions

Based on noise-free data and noise-containing data, we can estimate the parameters for erythropoiesis modeling in Table 2. The fitting results based on the two cases are shown in Figure 9. Corresponding RMSE are 0.0160 (no noise) and 0.0755 (with noise), respectively. The result shows these inferred parameters have a higher degree of accuracy. The agreement between the Hgb solution based on the estimated parameters and exact dynamics is good considering the noise in the training data.

## CONCLUSION

In this paper, we applied PINN technique to model the Hgb response under EPO treatment. This method combined physiological PK/PD model and neural network learning technology to estimate the parameters of PK/PD model. During the training of the neural network, physical laws describing the physiological model are enforced by adding the model residuals to the loss function. To address the problem that the PINN cannot easily handle the residual of the differential equation at the time instants with impulse inputs, we proposed an approximate model to replace the PK model equation. In addition, to handle the time delay in the PD differential equation, we proposed a weighting function-based formulation so that the delay parameter can be estimated by training the PINN. Tests on simulated data show that the proposed method has good prediction accuracy and is robust to noise.

The proposed modeling technique can help build individualized model for patients with renal disease. Physicians can rely on this modeling technique to develop patient-specific EPO dosing strategy to optimally manage the Hgb level of different patients. Future work can be done by integrating the PINN model into feedback control strategies to achieve this objective.

## ACKNOWLEDGEMENTS

This work was supported in part by the Natural Sciences and Engineering Research Council of Canada (NSERC).

## REFERENCES

1. Lankhorst CE, Wish JB. Anemia in renal disease: diagnosis and management. *Blood rev.* 24(1):39-47 (2010).
2. Hayat A, Haria D, Salifu MO. Erythropoietin stimulating agents in the management of anemia of chronic kidney disease. *Patient prefer. adher.* 2: 195 (2008).
3. Guyton A C, Hall J E. Textbook of medical physiology. *Philadelphia: Saunders* 548 (1986).
4. Bradbury BD, Danese MD, Gleeson M, Critchlow C. Effect of epoetin alfa dose changes on hemoglobin and mortality in hemodialysis patients with hemoglobin levels persistently below 11 g/dL. *Clin. J. Am. Soc. Nephrol.* 4(3):630-637 (2009).

5. Uehlinger DE, Gotch FA, Sheiner LB. A pharmacodynamic model of erythropoietin therapy for uremic anemia. *Clin. Pharm. Therap.* 51(1):76-89 (1992).
6. Ramakrishnan R, Cheung WK, Wacholtz MC, Minton N, Jusko WJ. Pharmacokinetic and pharmacodynamic modeling of recombinant human erythropoietin after single and multiple doses in healthy volunteers. *J. clin. pharmacol.* 44(9):991-1002 (2004).
7. Woo S, Krzyzanski W, Jusko WJ. Pharmacokinetic and pharmacodynamic modeling of recombinant human erythropoietin after intravenous and subcutaneous administration in rats. *J. Pharmacol. Exp. Ther.* 319(3):1297-1306 (2006).
8. Gaweda AE, Jacobs AA, Brier ME, Zurada, JM. Pharmacodynamic population analysis in chronic renal failure using artificial neural networks—a comparative study. *Neural Netw.* 16(5-6):841-845 (2003).
9. Gaweda AE, Muezzinoglu MK, Aronoff GR, Jacobs AA, Zurada JM, Brier ME. Individualization of pharmacological anemia management using reinforcement learning. *Neural Netw*. 18(5-6):826-834 (2005).
10. Shukla K, Jagtap AD, Karniadakis GE. Parallel physics-informed neural networks via domain decomposition. *J. Comput. Phys.* 447:110683 (2021).
11. Raissi M, Perdikaris P, Karniadakis GE. Physics-informed neural networks: A deep learning framework for solving forward and inverse problems involving nonlinear partial differential equations. *J. Comput. Phys.* 378:686-707 (2019).
12. Robinson S, Conteh FS, Oppong AY, Yellowhair TR, Newville JC, Demerdash NE, Shrock CL, Maxwell JR, Jett S, Northington FJ, Jantzie LL. Extended combined neonatal treatment with erythropoietin plus melatonin prevents posthemorrhagic hydrocephalus of prematurity in rats. *Front. Cell. Neurosci.* 12:322 (2018).
13. Chait Y, Horowitz J, Nichols B, Shrestha RP, Hollot CV, Germain MJ. Control-relevant erythropoiesis modeling in end-stage renal disease. *IEEE Trans. Biomed. Eng.* 61(3):658-664 (2013).
14. Chen H X, Mooney M, Boron M, Vena D, Mosby K, Grochow L, Jaffe C, Rubinstein L, Zwiebel J, Kaplan RS. Phase II multicenter trial of bevacizumab plus fluorouracil and leucovorin in patients with advanced refractory colorectal cancer: an NCI Treatment Referral Center Trial TRC-0301. *J. Clin. Oncol.* 24(21):3354-3360 (2006).
15. Duffus J. Glossary for chemists of terms used in toxicology (IUPAC Recommendations 1993). *Pure appl. chem.* 65(9):2003-2122 (1993).
16. Karniadakis GE, Kevrekidis IG, Lu L, Perdikaris P, Wang S, Yang L. Physics-informed machine learning. *Nat. Rev. Phys.* 3(6):422-440 (2021).
17. Yazdani A, Lu L, Raissi M, Karniadakis GE. Systems biology informed deep learning for inferring parameters and hidden dynamics. *PLoS comput. Biol.* 16(11):e1007575 (2020).
18. Bishop C M. Neural networks for pattern recognition. *Oxford university press* (1995).
19. Lu L, Meng X, Mao Z, Karniadakis GE. DeepXDE: A deep learning library for solving differential equations. SIAM Rev. 63(1):208-228 (2021).
20. Kingma DP, Ba J. Adam: A method for stochastic optimization. *arXiv preprint* arXiv:1412.6980 (2014).

This conference proceeding has not been peer reviewed.



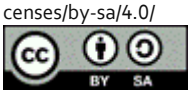


PSEcommunity.org
PSE Press ● Hamilton

Chemical Institute of Canada | ***For Our Future***
Institut de chimie du Canada | ***Pour notre avenir***